



HAL
open science

Seasonal and episodic runup variability on a Caribbean reef-lined beach

Thibault Laigre, Yann Balouin, Alexandre Nicolae-Lerma, Manuel Moisan,
Nico Valentini, D. Villarroel-Lamb, Ywenn De la Torre

► **To cite this version:**

Thibault Laigre, Yann Balouin, Alexandre Nicolae-Lerma, Manuel Moisan, Nico Valentini, et al.. Seasonal and episodic runup variability on a Caribbean reef-lined beach. *Journal of Geophysical Research. Oceans*, 2023, 128 (4), 10.1002/essoar.10511822.1 . hal-04057722v2

HAL Id: hal-04057722

<https://brgm.hal.science/hal-04057722v2>

Submitted on 27 Apr 2023

HAL is a multi-disciplinary open access archive for the deposit and dissemination of scientific research documents, whether they are published or not. The documents may come from teaching and research institutions in France or abroad, or from public or private research centers.

L'archive ouverte pluridisciplinaire **HAL**, est destinée au dépôt et à la diffusion de documents scientifiques de niveau recherche, publiés ou non, émanant des établissements d'enseignement et de recherche français ou étrangers, des laboratoires publics ou privés.

Seasonal and Episodic Runup Variability on a Caribbean Reef-Lined Beach

T. Laigre^{1,2} , Y. Balouin³, A. Nicolae-Lerma⁴, M. Moisan¹, N. Valentini³, D. Villarroel-Lamb² , and Y. De La Torre¹

¹BRGM, Parc d'activités Colin - La Lézarde, Petit-Bourg, Guadeloupe, France, ²The University of the West Indies, St Augustine Campus, St Augustine, Trinidad and Tobago, ³BRGM - Université de Montpellier, Montpellier, France, ⁴BRGM, Parc Technologique Europarc, Pessac, France

Key Points:

- A camera-derived time series of 2 years and 10 months is used to evaluate processes involved in daily maximum runup
- Storm-induced runup is highly modulated by annual sea-level periodicity and tidal level
- Upper beach vegetation reduces the daily maximum runup during storms

Correspondence to:

T. Laigre,
t.laigre@brgm.fr

Citation:

Laigre, T., Balouin, Y., Nicolae-Lerma, A., Moisan, M., Valentini, N., Villarroel-Lamb, D., & De La Torre, Y. (2023). Seasonal and episodic runup variability on a Caribbean reef-lined beach. *Journal of Geophysical Research: Oceans*, 128, e2022JC019575. <https://doi.org/10.1029/2022JC019575>

Received 14 DEC 2022
Accepted 28 MAR 2023

Author Contributions:

Conceptualization: T. Laigre, Y. Balouin
Formal analysis: T. Laigre, Y. Balouin, A. Nicolae-Lerma, M. Moisan, N. Valentini
Funding acquisition: Y. Balouin, Y. De La Torre
Investigation: T. Laigre
Methodology: T. Laigre, Y. Balouin, A. Nicolae-Lerma, M. Moisan
Project Administration: Y. Balouin, Y. De La Torre
Resources: Y. Balouin, Y. De La Torre
Software: T. Laigre
Supervision: Y. Balouin, D. Villarroel-Lamb, Y. De La Torre
Validation: Y. Balouin, A. Nicolae-Lerma, M. Moisan
Visualization: T. Laigre
Writing – original draft: T. Laigre, Y. Balouin

© 2023 The Authors.

This is an open access article under the terms of the [Creative Commons Attribution-NonCommercial License](https://creativecommons.org/licenses/by-nc/4.0/), which permits use, distribution and reproduction in any medium, provided the original work is properly cited and is not used for commercial purposes.

Abstract Many low-lying coastlines are exposed to overwash and marine flooding during large storm events, and the role of coastal ecosystems in reducing these hazards has been increasingly investigated and reported. This paper deals with the assessment of processes involved in coastal flooding over 2 years and 10 months at Anse Maurice, a reef-fringed pocket beach located in Guadeloupe Island, in the Caribbean region. Daily maximum marine inundation was assessed using a fixed video system, and a hydrodynamic measurement campaign was organized to monitor local wave transformation through the reef system. The results show that daily highest runups (dHRs) are not linearly correlated with storm events since storm runup intensity is highly modulated by (a) the steric-induced annual periodicity of sea level which showed minima in April and maxima in September and (b) the tidal level which influenced shortwave propagation on the reef flat (RF). These variables determined the reef submergence, an important parameter involved in wave transformation over reefs. Consequently, different runup responses existed for similar incident wave conditions, but generally wave attenuation ranged between 50% and 80%. Low-frequency waves were found to dominate the hydrodynamics on the RF for the most intense wave conditions. The upper beach vegetation also reduces the maximum swash excursion at the beach between 1.7% and 42.8% for the observed storms, and thus reduces the potential for back beach flooding. This study demonstrates new comprehensive elements on runup behavior and nearshore processes, at different time scales, on reef-lined beaches.

Plain Language Summary Small Caribbean islands are highly vulnerable to the coastal flooding hazard and the role of ecosystems in mitigating this hazard is increasingly emphasized. The physical processes involved in beach inundation were assessed at a reef-lined beach located in Guadeloupe Island in the Caribbean. Pluriannual data sets from a fixed camera and monthly hydrodynamic campaigns were used for this work which highlights the role of various processes involved in wave-induced coastal inundation (runup) from annual to hourly time scales. Seasonal variations in the expansion of water bodies (called steric expansion) which are triggered by fluctuations in temperature and salinity strongly control the wave runup. On shorter time scales, tides affect wave propagation over the coral reef, directly influencing the residual waves at the shoreline. Thus, low-frequency waves were found to dominate hydrodynamics on the reef flat for the most intense wave conditions. New results indicate that coastal inundation is greatly modulated by the annual periodicity of sea level, as well as, by tidal level at short time scales. Also, the study shows that the upper beach vegetation can reduce beach inundation. These results bring new elements to understanding wave-induced coastal inundation in the context of reef-lined beaches.

1. Introduction

The smaller islands of the Caribbean are highly vulnerable to coastal flooding since limited space and topographical constraints have oriented human development near coastal areas, and the Caribbean region is exposed to strong hydrodynamic events through North Atlantic winter swells (Hawkins et al., 2022) and cyclones (Rueda et al., 2017). However, most of the coastal flooding events occurring in the Caribbean are related to cyclones (Rueda et al., 2017) and the strength of these cyclonic events is anticipated to rise in the near future (Knutson et al., 2019; Torres & Tsimplis, 2014). In association with other effects of climate change like sea-level rise, the frequency, and intensity of storm-related or chronic flooding events are expected to increase in the next decades (Vitousek et al., 2017) with its concomitant impact on human assets (Ferrario et al., 2014).

Writing – review & editing: T. Laigre, Y. Balouin, A. Nicolae-Lerma, M. Moisan, N. Valentini, D. Villarroya-Lamb

Coastal floods are related to the total water level (TWL) reached at the coast (Sallenger, 2000), which is defined as the sum of the still water level (SWL) and the runup. Several forcings act on the SWL at different time scales. At the event time scale, astronomical tides, storm surge, and wind setup are the main contributing parameters. These short time scale processes are superimposed on lower frequency fluctuations which include eddies at a weekly time scale (Chelton et al., 2007; Torres & Tsimplis, 2014) and steric expansion at an annual time scale (Bindoff et al., 2007; Chelton & Enfield, 1986; Gill & Niller, 1973; Torres & Tsimplis, 2012) induced by water temperature and salinity on water bodies. Ocean oscillations like El Niño-Southern Oscillation (ENSO) and the North Atlantic Oscillation (NAO) also act on SWL at a pluriannual scale (Church, 2015; Enfield & Allen, 1980). In the Caribbean, extreme sea levels are mainly due to storm surge with a significant contribution from steric expansion variability and eddies (Torres & Tsimplis, 2014). Additionally, runup describes wave-induced water dynamics at the shoreline level. It is defined as the maximum onshore elevation reached by waves relative to the SWL. Runup is the sum of wave setup, the time-averaged water level at the shoreline position (steady component) and swash, the instantaneous water level materialized by bore-like waves on the beach (dynamic component) (Baldock, 2012; Pomeroy et al., 2012; Stockdon et al., 2006). On open coasts, runup is primarily correlated with the incident wave energy and second to the foreshore and beach morphology (Guedes et al., 2011; Nicolae Lerma et al., 2017). On reef-lined beaches, the processes associated with runup are more complex and highly dependent on reef properties (Buckley et al., 2018). Fringing coral reef systems provide numerous ecosystem services and, in particular, wave energy dissipation (Gerritsen, 1980; Harris et al., 2018; Lowe et al., 2005). Coral reefs could dissipate up to 97% of the incident wave energy (Ferrario et al., 2014), where the magnitude of dissipated energy depends on the reef morphology and the hydrodynamic forcing. Metamodels have been developed to predict runup response in a wide panel of reef settings. It appears that waves, water levels, and the reef width are the main parameters involved in the extent of back-reef inundation (Pearson et al., 2017; Rueda et al., 2019).

SWL variations change the water depth over the reef, which is the main parameter influencing wave attenuation and leads to a subsequent response of the runup (Becker et al., 2014; Cheriton et al., 2016; Ning et al., 2018; Wandres et al., 2020). Shallower reefs contribute to more efficient wave energy dissipation and deeper reefs are less efficient. Moreover, a fraction of the incident wave energy which is mostly comprised of short waves (SW, typical wave frequency > 0.04 Hz) is transferred to lower frequencies, generating infragravity (IG) waves ($0.004 < \text{wave frequency} < 0.04$ Hz) and very low-frequency (VLF) waves (wave frequency < 0.004 Hz) (Cheriton et al., 2016, 2020; Péquignet et al., 2009). Energy transfer to the IG band is mainly dependent on (a) breakpoint forcing on the reef crest (RC), which is linked to the variation in wave setup induced by wave groups generating a setup wave in phase with group waves (Symonds et al., 1982) and (b) the release of free bound waves associated with the SW envelope during wave breaking (Longuet-Higgins & Stewart, 1962). This transformation may lead to low-frequency dominance of the runup signal (Ford et al., 2013; Quataert, 2015; Quataert et al., 2020; Roeber & Bricker, 2015). This switch in energy frequency bands strongly depends on hydrodynamic conditions and morphological characteristics of the reef platform (Masselink et al., 2019), and is commonly observed at reef-lined beaches.

Video systems are nowadays widely used to evaluate coastal evolution and hydrodynamics, allowing for the quantitative acquisition of optical signatures of shoreline position (Holman & Stanley, 2007; Plant et al., 2007; Valentini et al., 2020), nearshore morphologies (Aarninkhof & Ruessink, 2004; Bergsma & Almar, 2018), wave characteristics (Almar et al., 2008), surf zone wave-induced current (Rodríguez-padilla et al., 2021), and wave runup (Salmon et al., 2007; Valentini et al., 2019). Recently, low-cost webcams have been increasingly used (Andriolo et al., 2019; Paquier et al., 2020; Valentini et al., 2020) and have proven their ability to acquire reliable data at an affordable price. In this study, a video system was used to extract daily maximum inundation over 2 years and 10 months (1,045 days). High-frequency in situ runup and TWL observations over long periods are scarce in reef environments. A recent study presents a 1-year runup data set on a sandy beach (Melito et al., 2022) but to the authors' knowledge, no study proposes a continuous multiyear data set providing analysis of runup variability at a daily to a pluriannual time scale.

This study presents a novel investigation into the complex interaction between the parameters that impact TWL in a reef-fringed pocket beach context. Utilizing a combination of pluriannual in situ observations from cameras and monthly hydrodynamic measurements, the study aims to provide new insights into the runup variability, hydrodynamic conditions, wave transformation on the reef, and the impact of vegetation on swash reduction. This approach addressing the variables that influence TWL over an extended period of time and connecting these to

short-term processes has never been undertaken before and provides an opportunity to gain new insights into the complex processes affecting TWL in this environment.

The study has three objectives aiming to assess on the TWL dynamics in a new and innovative way: (a) to analyze the pluriannual runup variability and its relationship with sea level and incident wave conditions; (b) to examine the role of different components such as wave setup, swash, IG, and VLF waves in daily TWL (dTWL) fluctuations; and (c) to evaluate the variability of vegetation limits and its impact on swash reduction.

2. Study Area and Methodology

2.1. Study Site Description

Anse Maurice is located on Guadeloupe Island (France) in the Lesser Antilles (Figures 1a and 1b). It is a small beach, about 200-m long and between 5-m and 20-m wide. Shoreline monitoring indicates the beach is undergoing chronic erosion with a net retreat of 20 m, on average, between 1950 and 2013 (Guillen et al., 2017).

The beach is bordered by a fringing reef mainly composed of *Acropora palmata* dead colonies covered by algae. However, some complex structures of several meters in height are still observed (Figure 1e). The reef flat (RF) is composed of discontinuous dead coral structures of about 1 m in height and several meters in width, as well as, small colonies of living branching and encrusting corals. In the southern part of the site, a channel is identifiable where the coral structures are sparser and deeper (Figure 1b).

The upper beach is covered by heterogeneous patches of vegetation: crawling vegetation mainly represented by *Ipomoea pes-caprae* in the front line and shrubs like *Coccoloba uvifera* in the back line (Figure 1d). Several exogenous coconut trees are also present on the site.

Beach vegetation at the Anse Maurice site is very impacted by human activities, and particularly by trampling and goat grazing. Lower layers of vegetation are the most affected, which obstruct the development of crawling vegetation and seedlings. Consequently, in the medium-term, the growth of a new generation of trees is being hampered and the soil is more subject to erosion. Therefore, the French Forestry Agency (ONF) has implemented several revegetation enclosures which consist of simple wooden sticks connected by wire mesh to avoid human trampling and goat grazing, and facilitate the recovery of vegetation. After a few months, the effects are visible and dense vegetation can be restored after a few years (Ellison, 2018; Johnston & Ellison, 2014). Even in a deteriorated state, the role of the reef and the upper beach vegetation on coastal flooding attenuation is anticipated, although this has not yet been locally evaluated.

The site is on a wave-dominated shore where offshore swells vary greatly with an annual mean wave height of 1.2 m. It is exposed to strong Atlantic swells with most of the storms occurring during the winter from December to March; these swells mainly originate from the North to East-North-East direction (Hawkins et al., 2022). The site is also subject to cyclonic events from July to November, which can generate the most intense waves that reach the island with wave height that may exceed 10 m. Nevertheless, due to the site's orientation, only swells from the North to East direction impact it directly. Besides these two highly energetic wave regimes, waves generated by the trade winds affect the region all year round with wave heights ranging from 0.5 to 2 m (CEREMA, 2021; Reguero et al., 2013). The flooding risk is primarily associated with the occurrence of tropical cyclones (Krien et al., 2015).

The area exhibits a semidiurnal microtidal range, with diurnal and mixed inequality, a mean magnitude of 0.25 m, ranging from 0.1 m during neap tides to 0.6 m during spring tides (SHOM, 2020). Additionally, sea level depends on nontidal forcings. At the event scale, atmospheric pressure and wind may have a significant impact (storm surge). At the seasonal scale, forcings like atmospheric pressure and steric expansion cycles may influence the sea level. Annual variations in atmospheric pressure in the Caribbean are due to the movement of the Inter-Tropical Convergence Zone (ITCZ) but in Guadeloupe, the impact on sea level is considered insignificant (<0.01 m). Most of the annual sea-level variations are the consequence of steric effects with a magnitude of 0.16 m on the island of Guadeloupe, having a maximum value in October and minimum value in April (Torres & Tsimplis, 2012).

2.2. Offshore Hydrodynamic Data Sets

Offshore wave conditions were extracted from the mesoscale MARC (<https://marc.ifremer.fr/>) model outputs which is available online. MARC is a reanalysis of the WAVEWATCH III® model at a regional scale; simulation

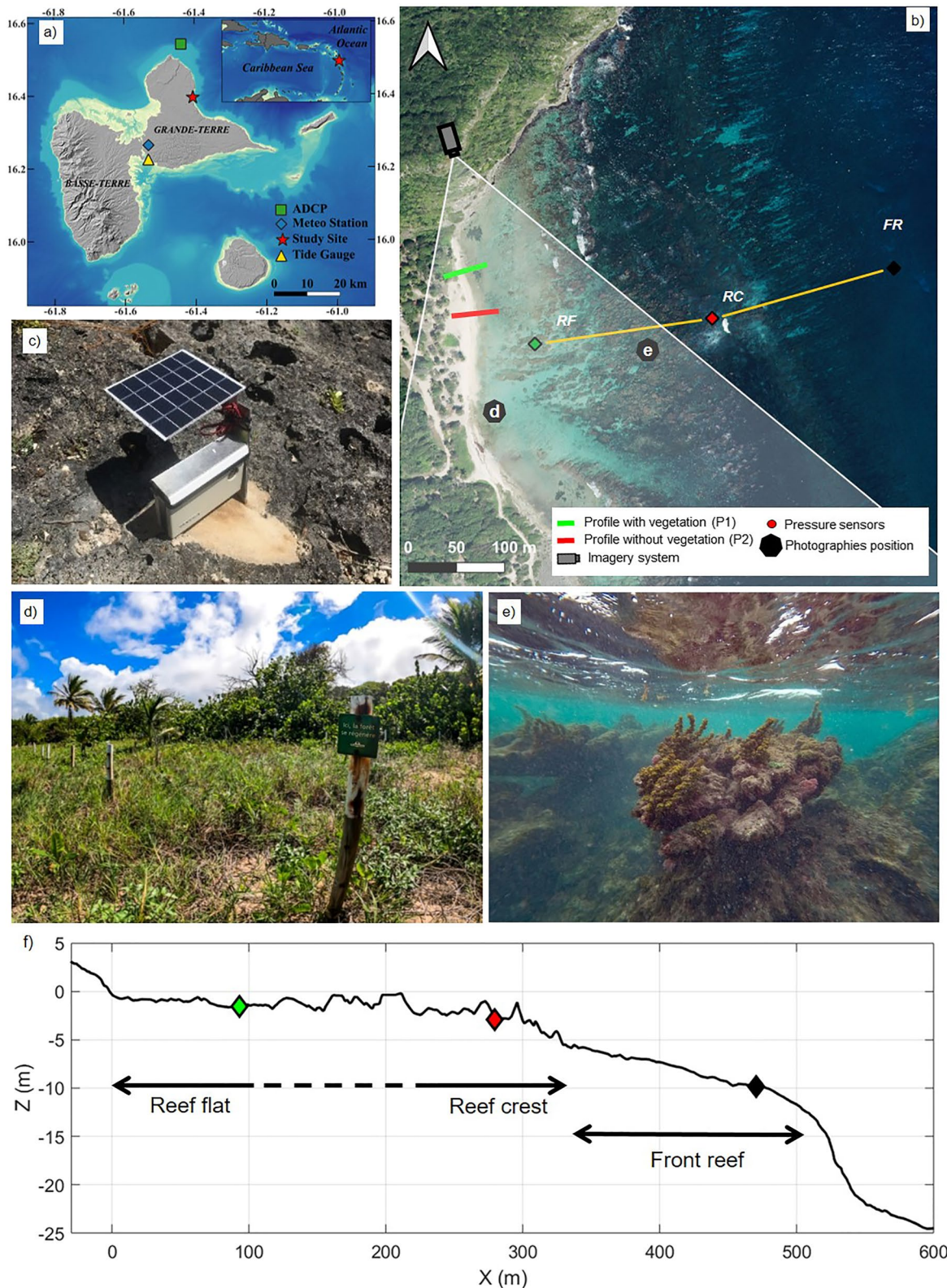


Figure 1. (a) Location of Guadeloupe Island in the Caribbean and the Anse Maurice beach (red star) on the East coast of the Island. Markers indicate the location of the regional data sets: ADCP (green square), meteorological station (blue diamond), and tide gauge (yellow triangle). (b) Anse Maurice beach orthophotography with the location of instruments, extracted profiles from camera and position of pictures (d) and (e). (c) Imagery system installed at Anse Maurice, its position on-site is presented on (b). (d) Upper beach vegetation at the Anse Maurice. (e) Anse Maurice reef crest (RC) showing a dead *Acropora palmata* colony covered with algae. (f) Instrumented cross-reef profile with reef flat (green), RC, (red), and front reef (black) sensors.

Table 1
Sensors Set Up During the Hydrodynamic Field Data Campaign

Sensor name	Deployment period	Active duration (days)	Burst sampling	Frequency (Hz)	Depth (m)	Relative distance to reef crest (m)
FR	Aug-Sept 2021	37	1 burst/hour	2	8.9	−200
RC	Aug-Sept 2021	37	1 burst/hour	2	2.7	0
RF	Aug-Sept 2021	37	1 burst/hour	2	1	175
ADCP	Aug-Dec 2020	122	1 burst/hour	2	50	−

Note. Nearshore pressure sensor names correspond to the position over the reef and year (FR: front reef, R: reef crest, RF: reef flat).

results are provided by the IFREMER (Institut Français de Recherche pour l'Exploitation de la Mer) and available in real time (<https://marc.ifremer.fr/resultats/vagues>). An acoustic doppler current profiler (ADCP) was installed to the North of the site and used for wave model validation (Figure 1a). The ADCP (©Nortek Aquapro) was installed at 50-m water depth to measure offshore waves from September to December 2020 (Table 1). Wave parameters (significant wave height— H_s , peak period— T_p , and direction at the peak— D_p) were extracted from the MARC model at the location of the ADCP, for data validation. Although there is a strong H_s correlation between the ADCP measurements and the MARC model ($R^2 = 0.90$), there exists a difference which depends on the wave conditions (a greater variance was observed in extreme wave conditions). This observation is common when comparing instrument data with models (e.g., Castelle et al., 2015). It was decided to apply a correction method to the distribution of wave conditions and thus, a quantile-by-quantile correction has been applied. Quantile-by-quantile correction is a useful tool in wave data analysis because it helps to ensure that the data being analyzed conforms to the assumed distribution, and allows for the detection of potential anomalies or outliers in the sample data. Rather than using a single affine correction value, this technic applies a different affine correction equation for each quantile, it is thus an effective manner to reduce bias for wave model data sets which may underestimate or overestimate storm intensity (Charles et al., 2012). The overall correlation slightly increases after the correction ($R^2 = 0.92$). The ADCP's position may potentially be exposed to waves originating from the west, whereas the study site's location may only be exposed to swell from north (0°) to south (180°) directions. However, waves from the west are rare, and only a hurricane with a specific path could produce such wave directions. Thus, identifying and filtering these waves would be simple, but the situation was not observed during the measurement period.

Daily maximum wave parameters were extracted from the corrected MARC model outputs. The daily H_s maximum value was extracted, along with the T_p and D_p at the time of the maximum wave height. A daily maximum value of sea level from the Pointe-à-Pitre tide gauge (Figure 1a) was also extracted following the same methodology. Data from the tide gauge data are provided by the French Hydrographic Service (SHOM) and are available on the REFMAR database ([www.http://data.shom.fr](http://data.shom.fr)). Since the tide gauge is located away from the study site, additional analysis was conducted to determine its consistency with the on-site sea level. The tide gauge data were compared to the data from a pressure sensor placed on the front reef (FR; not shown here), not evidencing any phase lag. The only discrepancy between the pressure sensor data set and the tide gauge was noticed during periods of strong waves, when shoaling at the sensor location could affect the mean water level.

Figure 2 presents the offshore waves and SWL over the 1,045 days corresponding to the period of camera observations. The method used by Masselink et al. (2016) was applied to detect and isolate storms in the corrected MARC model data set. Thus, in the H_s data set, the percentile 95% ($H_{s,95\%}$) was extracted where events exceeding $H_{s,95\%}$ were considered to be a storm. The upcrossing and downcrossing on the 75% percentile define the beginning and end of the storms.

Offshore H_s exceeded $H_{s,95\%}$ 20 times (where $H_{s,95\%} = 2.9$ m and $H_{s,75\%} = 2.2$ m), with three of these events over 4 m. The first of these three events corresponded to a winter swell storm with a peak on 10 January 2020, and the two others were cyclonic events peaking on 20 July 2020, and on 20 September 2020. The 20 September event was related to Hurricane Teddy circulating at 800 km to the East of Guadeloupe Island (NHC, 2021).

Figure 2b presents the global SWL variations from the Pointe-à-Pitre tide gauge. For further analysis, the two components of the tide were extracted. The astronomical tide was extracted from the TPX09-atlas ($1/30^\circ$

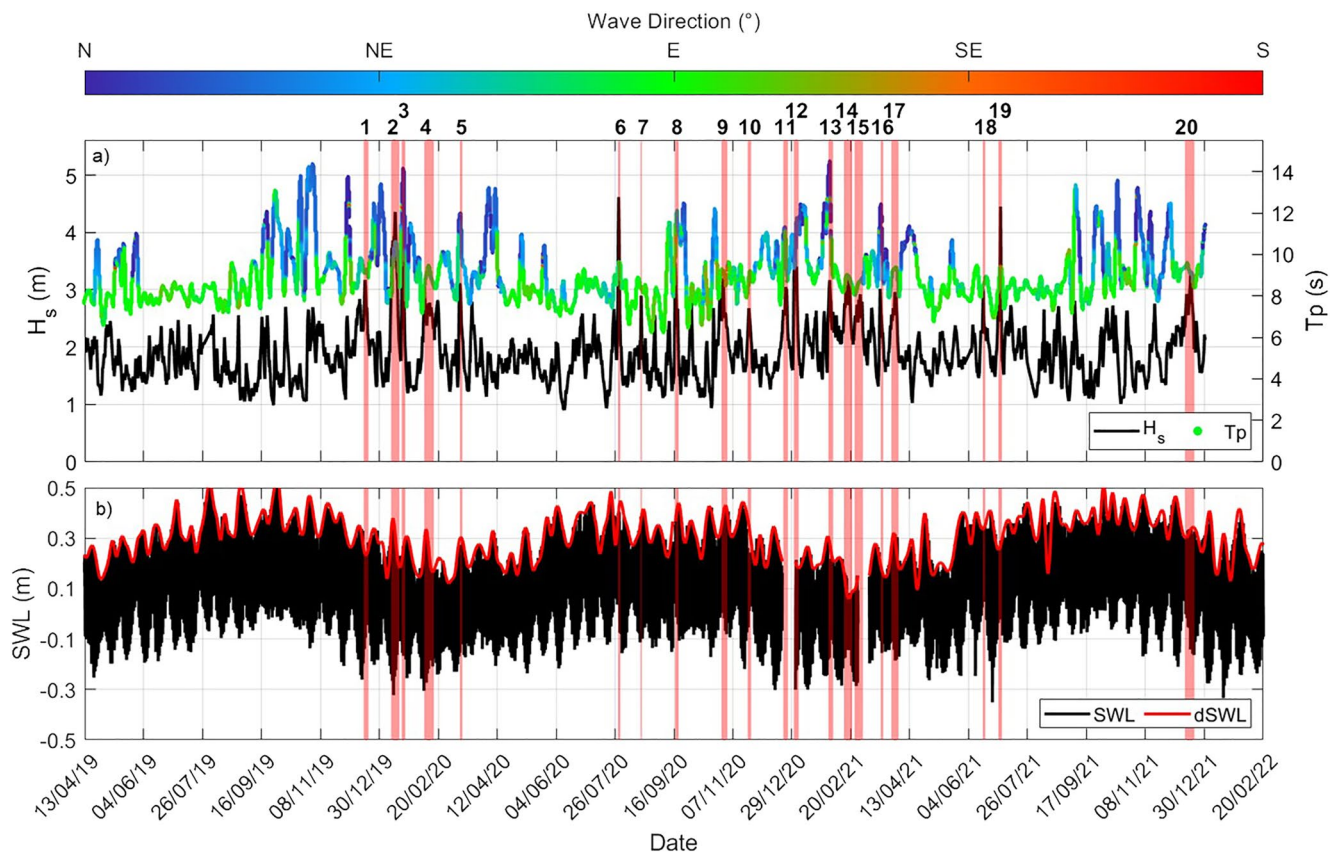


Figure 2. Wave and sea-level conditions from April 2019 to February 2022. (a) Offshore significant wave height (H_s) and peak period (T_p) with associated wave mean direction (D_p) represented by the color of T_p points. (b) Sea-level variations on Pointe-à-Pitre tide gauge (SWL) and daily maximum (dSWL).

resolution) database (Egbert et al., 1994) and the anomalies were calculated as the difference between the global SWL and TPXO tide.

For each storm event, the cumulative wave power in kWh/m was calculated as in Splinter et al. (2014). This analysis gives more information than the peak conditions by associating the temporal and the hydrodynamic dimensions. It is defined as follows:

$$\Sigma P = \int_0^N P \Delta t$$

where N is the event duration and P is the wave power per meter of wavefront length in kW/m, defined as

$$P = \frac{\rho g^2}{64\pi} H_s T_p$$

where ρ is the water density and g is the acceleration due to gravity.

2.3. Field Measurements

2.3.1. Video-Derived Coastal State Indicators

In this study, a low-cost (~400 USD) Solarcam[®] camera systems were implemented in April 2019 to monitor coastal evolution (Figures 1b and 1c). The system comprised an 8-MP resolution smartphone protected by a waterproof housing and powered by a solar panel. The whole system was entirely autonomous as it was programmed to record an image every 10 min and can also record short videos (Valentini et al., 2020). This low-cost device showed its applicability for several purposes (Moisan et al., 2021; Valentini et al., 2020) but it is inadequate to study nearshore hydrodynamics as it cannot record videos with sufficient duration and frequency.

A data set of 2 years and 10 months (1,045 days) has been analyzed where the images from the cameras were calibrated with ground control points using the Holland et al. (1997) methodology to obtain data on a real-world scale. This rectification processing allows the transformation of U , and V image coordinates to X , Y , and Z world coordinates and allows the quantitative assessment of coastal indicators. After rectification, timestacks were generated corresponding to the location of profiles (Figure 1b). A timestack represents the plotted evolution over time of a particular line of pixels. Morphological markers like the limit between sand and vegetation, or the limit formed by marine debris are easily identifiable on images and may be monitored over time with timestacks. For example, brown patterns located at the limit between sand and water (i.e., the shoreline) are sargassum algae deposits. Those are effective markers of maximum swash events on timestacks because they present a clear colorimetric contrast with the sand. A better precision was obtained by detecting the swash limit on raw oblique images rather than timestacks because of their rapid evolution. Vegetation limit evolution is more stable and was directly extracted from the timestacks. This data is useful for identifying instantaneous swash position, potentially generating a back beach inundation indicator. In order to deduce the TWL, the position of the swash limit on the profile was correlated with the local Digital Elevation Model (DEM). The DEM was derived from RTK-GPS monitoring for the topography and the Lidar data set (SHOM, 2016) for the bathymetry. The elevation was then expressed in the local reference system (IGN88) and the dTWL was identified and extracted. It is important to note that in the case of massive sargassum algae beaching, which may occur from May to September (Moisan et al., 2021), the TWL detection from the camera is hampered. The presence of sargassum induces an extraction of the swash position further offshore than the actual shoreline position, thus the resulting TWL may be less than the SWL, which is impossible. Therefore, TWL values less than the SWL values are removed from the data set. This bias only appears for calm conditions as sargassum returns to the sea with more energetic conditions. Subsequently, in order to obtain the daily highest runup (dHR) value, the daily maximum SWL (dSWL) is subtracted from the dTWL.

In this study, two timestacks will be used and compared. The first one is along a profile with dense upper beach vegetation (the northern profile line in Figure 1b, hereafter called P1) and the other along a profile with limited upper beach vegetation (hereafter called P2). The mean pixel resolution on each profile is, respectively, 0.15 and 0.19 m. The profiles were selected so that certain characteristics remain consistent along each profile. The topography along of each profile is similar, as well as, they are comparable with respect to longshore direction. Therefore, it is assumed that reef variability did not generate significant differences in nearshore hydrodynamics between the two profiles. The attenuation percentage was calculated as the dHR percentage of difference between the two profiles with P2 as reference and was calculated as follows:

$$\text{Attenuation} = \frac{\text{dHR}(P2) - \text{dHR}(P1)}{\text{dHR}(P2)} * 100$$

Additionally, the relative vegetation limit (RVL) was calculated and corresponds to the vegetation elevation relative to the dSWL position. This variable reflects the vegetation's vulnerability to runup.

2.4. Wave Measurements

A campaign of hydrodynamic measurements was organized during the 2021 North Atlantic cyclonic season. The sensor positions for the hydrodynamic data collection were chosen according to the reef characteristics so that data can be collected at, and compared to various cross-shore positions relative to the reef. The campaign started on 26 August and lasted until 01 October 2021 (37 days). Three Wisens Wave[®] pressure sensors (NKE instrument[®]) were installed along a cross-shore profile (see Figure 1b): the first one on the FR, the second one on the RC, and the last one on the RF.

The three pressure sensors and the ADCP were set up to record bursts of 2,048 readings at a sampling frequency of 2 Hz (~17-min duration) every hour. Table 1 details the setup of the pressure sensors.

For the wave parameter extraction from the sensor data, the effect of atmospheric pressure on raw pressure records was removed using 3-hourly data from the MétéoFrance station located at le Raizet Airport which is ~20 km from the study site (Figure 1a). Using filtered data sets, the one-dimensional frequency spectra, $S(f)$, was estimated using Welch's averaged periodogram method with windows of half burst length and 50% overlapping. Finally, for each burst and within the SW, IG, and VLF frequency bands, several statistical parameters

were extracted. Cut-off frequencies were chosen based on previous studies where the SW band corresponds to frequencies between 0.04 and 0.2 Hz, the IG band corresponds to frequencies between 0.04 and 0.004 Hz and the VLF band corresponds to frequencies below 0.004 Hz (Cheriton et al., 2016, 2020; Péquignot et al., 2009; Quataert et al., 2020). Also, the root-mean-squared wave height (H_{rms}) was described using the following equation:

$$H_{\text{rms}} = \sqrt{8 \int_{f_2}^{f_1} S(f) df}$$

with f_1 and f_2 being the lower-frequency and upper-frequency limits, respectively. The peak period, T_p , value for each band represents is $1/f_p$ where f_p is the frequency associated with the peak of wave energy. The H_{rms} transmission coefficient between the FR and the RF was also calculated for each frequency band. It represents the ratio of H_{rms} measured by the sensors on the RF (transmitted wave) and H_{rms} measured by the sensors on the FR (incident wave) (Costa et al., 2016; Escudero et al., 2020; Lugo-Fernández et al., 1998). The transmission is expressed as a percentage, where values smaller than 100% reflect an attenuation between the FR and the RF, and values greater than 100% reflect an amplification.

The wave setup on the RF was also extracted from the measurements and calculated the methods in Vetter et al. (2010)

$$\eta = h_{rf} - h_{fr} - (bt + c)$$

where η is the wave-induced setup on the RF, h_{rf} , and h_{fr} are, respectively, the burst-averaged water levels for the RF and the FR sensor; b and c are the coefficients that empirically chosen and are used to, respectively, account for any drift of the pressure transducers over time and offset.

Statistical analyses were performed to identify and quantify the dependency between variables. The squared Pearson correlation coefficient, R^2 , was calculated when comparing two linearly correlated random variables with a linear distribution (such as H_{rms} , T_p , or sea level) defined in Fisher (1958) as follows:

$$R^2(A, B) = \left(\frac{1}{N-1} \right) \sum_{i=1}^N \left(\frac{A_i - \mu_A}{\sigma_A} \right) \left(\frac{B_i - \mu_B}{\sigma_B} \right)^2$$

where A and B are the random variables, N is the number of observations, μ_A is the mean of A and μ_B is the mean of B , σ_A is the standard deviation of A , and σ_B is the standard deviation of B .

In order to compare a linear random variable with a circular random variable (such as D_p), a circular-linear correlation was performed as defined in Mardia and Jupp (2000) as the following:

$$R^2(A, \theta) = \frac{r_{Ac\theta}^2 + r_{As\theta}^2 - 2r_{Ac\theta}r_{As\theta}r_{cs\theta}}{1 - r_{cs\theta}^2}$$

with

$$r_{Ac\theta} = \text{corr}(A, \cos \theta)$$

$$r_{As\theta} = \text{corr}(A, \sin \theta)$$

$$r_{cs\theta} = \text{corr}(\sin \theta, \cos \theta)$$

where A and θ are, respectively, the linear random variable and the circular random variable.

Both the coefficients of the linear (Pearson) and the circular-linear correlation range between 0 and 1, and the association between variables is stronger with greater values. In this study, correlations above 0.2 were considered significant and correlations above 0.6 as strong. All correlations presented have a p -value < 0.05 and exceptions to this are specifically mentioned.

A sinusoidal fit was also applied to the daily time series to detect annual cyclicity. This sinusoidal fit was obtained by fitting a least-squares estimate of a sinusoid that has a periodicity of 1 year to the data set (Greene et al., 2019).

3. Results

3.1. Pluriannual Video Observations

3.1.1. Pluriannual Evolution of the dTWL and dHR

Figures 3a and 3b present timestacks over the same period at the two cross-shore locations represented by the red and green lines in Figure 1b. As mentioned in Section 2.3.1, the timestack of the northern profile is located in an area with dense upper beach vegetation mostly comprising *Ipomoea pes-caprae*. The timestack on the southern profile is in an area where upper beach vegetation is less developed and is located more landward due to human trampling. The vegetation limit and the maximum swash excursion are also plotted. The vegetation, only present on the timestack of the northern profile, shows an evolution in vegetation density which is displayed as variations from a green to yellowish color behind the vegetation limit. The vegetation limit on the coastal border (plotted in green in Figure 3a) shows slow growth periods interrupted by abrupt retreats. Two remarkable changes appear with net retreats of 3 and 4 m which are both linked to larger values of the dTWL (Figure 3c). The first retreat occurred at the end of July 2020 in correlation with storm event number 6 and the second in mid-September 2021 with no direct storm correlation (refer to Table 2).

Table 2 compiles the storm conditions (Figure 2) and the associated observed dTWL (Figure 3). It appears that storms correlated with cyclonic events are shorter in duration (a mean of 2.7 days) than the winter storm events (a

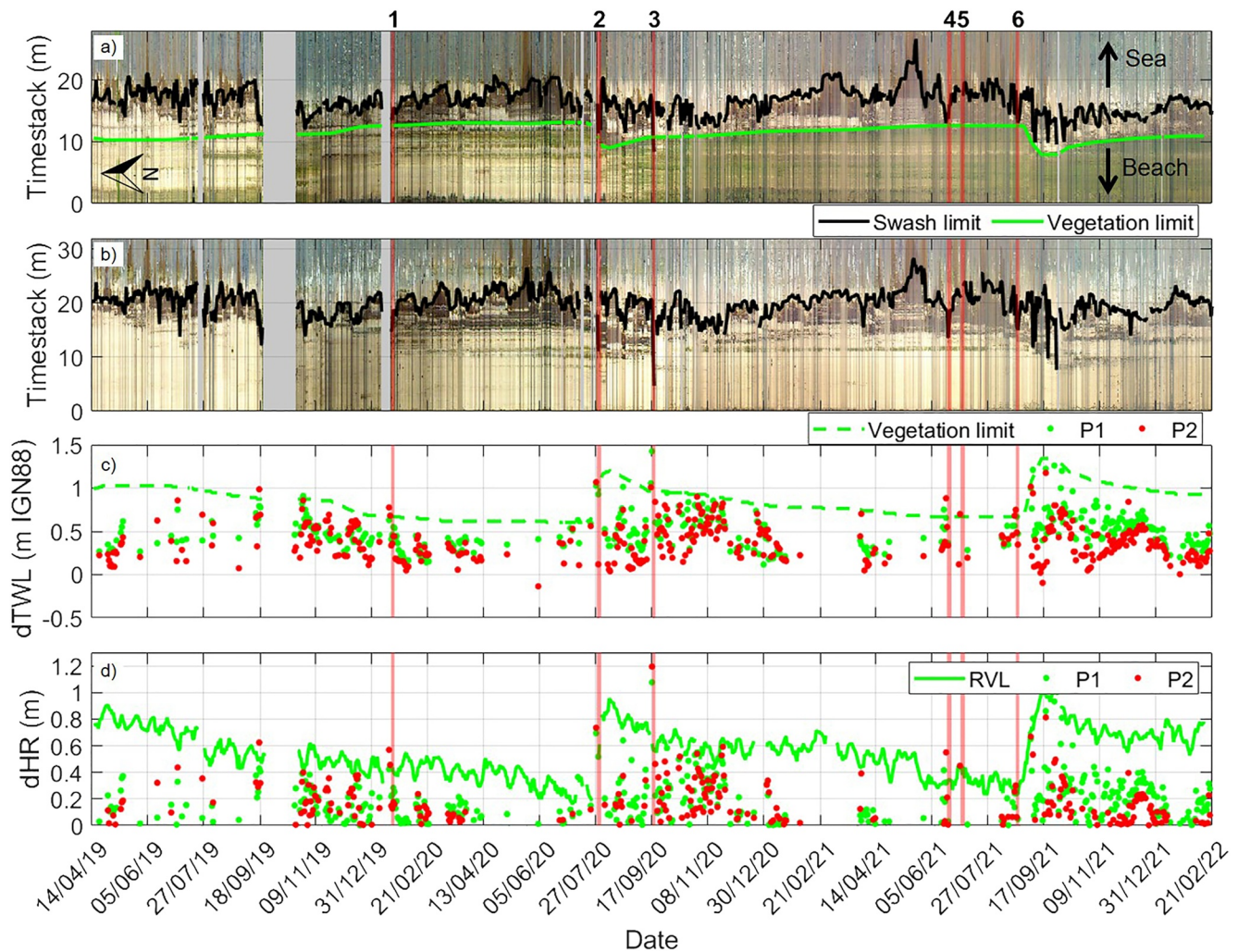


Figure 3. The camera-derived observations from April 2019 to February 2022. (a and b) Daily timestacks with detection of maximum swash limit (black line) and vegetation limit (green line) on P1 (beach backed by vegetation) and P2 (no upper beach vegetation), respectively. (c) Evolution of the daily total water level (dTWL) on both profiles, with vegetation limit height on P1. (d) Evolution of the dHR on both profiles and relative vegetation limit (RVL). Events when the vegetation limit is surpassed by daily highest runup (dHR) are highlighted with a red background.

Table 2
Parameters Associated With Storms Observed During the Study Period Where the Darker Coloring Indicates the Higher Data Values and “nd” Means No data

Event id	Season	Peak date	Duration (days)	ΣP (kWh/m)	Peak conditions			dTWL (m)	
					H_s (m)	T_p (s)	D_p (°)	P1	P2
1	Winter	12/17/19	3.6	12.4	3.2	9.4	77	0.5	0.6
2	Winter	01/13/20	7.1	44.0	4.4	10.8	54	nd	nd
3	Winter	01/19/20	2.6	18.0	3.8	13.7	357	0.7	0.8
4	Winter	02/08/20	8.9	26.9	3.2	8.6	80	nd	nd
5	Winter	03/10/20	2.5	11.4	3.1	12.3	354	nd	nd
6	Cyclonic	07/29/20	2.0	13.0	4.6	11.1	76	1.0	1.1
7	Cyclonic	08/18/20	0.4	1.1	2.9	9.0	101	0.6	0.6
8	Cyclonic	09/19/20	2.9	13.0	3.0	9.3	81	1.4	1.5
9	Cyclonic	10/30/20	5.4	16.5	3.1	9.4	78	0.9	0.9
10	Cyclonic	11/21/20	3.0	9.0	2.9	9.2	81	0.6	0.7
11	Winter	12/24/20	4.6	16.7	3.1	12.0	358	nd	nd
12	Winter	01/01/21	3.9	19.9	3.6	9.2	38	0.6	0.5
13	Winter	02/01/21	3.8	17.6	3.2	13.5	353	nd	nd
14	Winter	02/18/21	7.0	24.1	3.2	8.8	76	nd	nd
15	Winter	02/28/21	7.3	20.9	2.9	14.7	1	nd	nd
16	Winter	03/18/21	2.3	9.7	3.0	13.3	355	nd	nd
17	Winter	03/31/21	5.8	17.9	3.0	9.1	84	0.4	0.4
18	Cyclonic	06/17/21	1.8	5.0	3.0	8.6	82	0.7	0.3
19	Cyclonic	07/02/21	3.6	15.0	4.5	10.6	105	0.6	0.7
20	Winter	12/08/21	8.3	28.2	3.3	9.8	61	0.7	0.6

mean of 5.2 days). Event number 8, peaking on 19 September 2020, is the most extreme with respect to shoreline response with a maximum swash excursion of 12 m inland and a corresponding dTWL exceeding 1.5 m on P2. This event was due to the passage of hurricane Teddy offshore of Guadeloupe Island. Overall, six significant swash excursion events were identified on both timestacks where all occurred during the cyclonic season. Storms that occurred during the winter, even the most extreme ones as event number 4 in January 2020, did not generate a major swash excursion.

Figure 3d presents the evolution of the dHR parameter on both the P1 and P2 profiles (see Section 2.3.1 for dHR extraction methodology) as well as the RVL. The RVL evolution is characterized by a progressive lowering over long periods and sharp and rapid increases and varied from 0.2 to 1 m. Thus, when the RVL is at its minimum value (i.e., larger vegetation cover on the lower beach), runup values from 0.2 m may reach the vegetation limit, while when the RVL is at its maximum, only runup values greater than 1 m may reach the vegetation.

3.1.2. dHR and Offshore Conditions Variability

In order to evaluate the relationship between offshore conditions and the local dHR, a series of linear regressions were performed. For these analyses, only data from profile line, P2, were used to avoid the potential effect of vegetation.

The linear correlations between the dHR extracted from the camera and the offshore daily hydrodynamic parameters showed a very poor relationship between offshore waves variables and the dHR, while a greater dependency with the sea level was observed ($R^2 = 0.42$, Figure 4).

As the correlation with the SWL is significant, the correlations with SWL components, the astronomical tide harmonics (dTide) and anomalies (dSWL anomalies) were calculated. The dTide omits high-frequency tidal undulations (e.g., semidiurnal cycles) but the cycles of lower frequencies are visible (e.g., neap and spring tide cycles). Also, the range of the dTide parameter is limited (~ 0.1 m) when compared to the range of the SWL

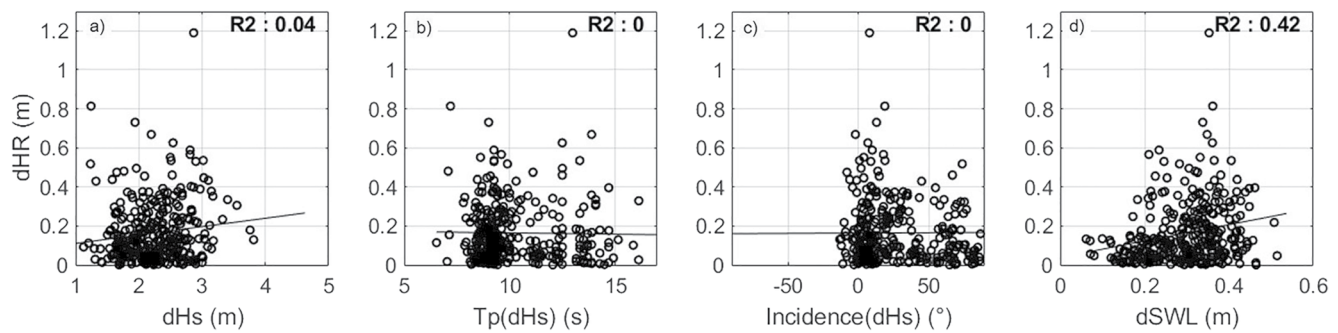


Figure 4. Linear regressions of daily highest runup (dHR) and (a) H_s , (b) T_p , (c) wave incidence (positive southwards), and (d) still water level (SWL).

anomalies (~ 0.35 m). Although there is a wide dispersion, the correlation between the dHR and the dSWL anomalies is significant ($R^2 = 0.56$) (Figure 5b).

In order to further analyze this relationship between the dSWL anomalies and the dHR temporally, a sinusoidal fit was performed to consider a potential seasonal cyclicality. The sinusoidal fit showing the best agreement with data has an annual period (365.25 days/cycle) and is presented in Figure 6 for the wave power, the dSWL anomalies, and the dHR. The phase of the annual signal corresponds to the period in days from the first of January to the peak of the sinusoid.

The results reveal that the cyclicality of the dHR and dSWL anomalies are similar in phase and amplitude, while the wave power exhibits an almost antiphased oscillation. The cumulative wave power shows an annual sinusoidal fit peaking in mid-January (phase: $14.5/365.25$), the SWL anomalies and the dHR annual fits show a very close peak around mid-September (phase: $253.5/365.25$ and $250.5/365.25$, respectively). The amplitudes of these two latter parameters are also very close, with both having a value of 0.17 m. Note that the R^2 of the annual sinusoidal fit for the SWL is strong (0.8) which suggests a strong annual control of those anomalies. The R^2 of the annual sinusoidal fit for the dHR is weaker (0.37) suggesting the implication of other contributing forcings. However, this good agreement between the pluriannual dHR evolution and the SWL anomalies annual cycle suggests that the regional sea-level anomalies have a larger influence than wave seasonality on runup behavior.

3.1.3. dHR and Vegetation Limit Variability

The dHR values were compared on both profiles during events exceeding the vegetation limit to highlight the potential effect of the vegetation layer. On both profiles, the mean values of the TWL are similar (mean difference of 0.02 m), but there is a significant difference only when the vegetation limit is exceeded. Figure 7 presents the dHR on P1 and P2 associated with the six events exceeding the vegetation limit. Table 3 compiles

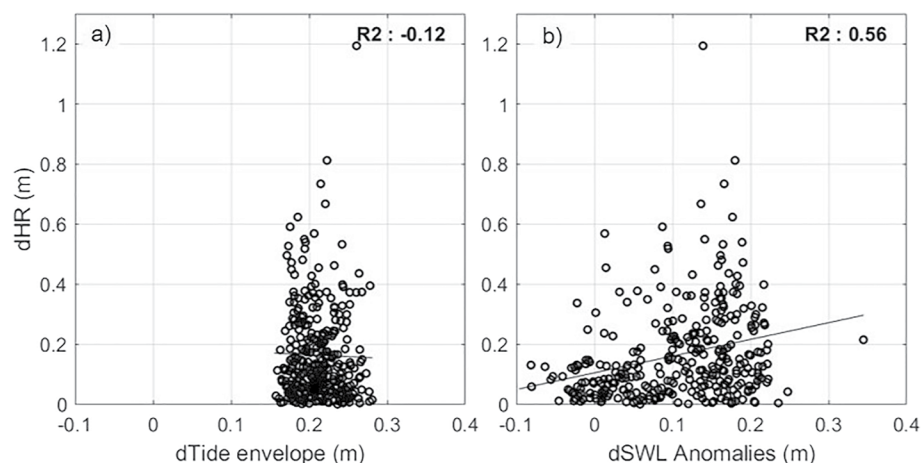


Figure 5. Linear regression of the daily highest runup (dHR) and (a) tide envelope and (b) the still water level (SWL) anomalies.

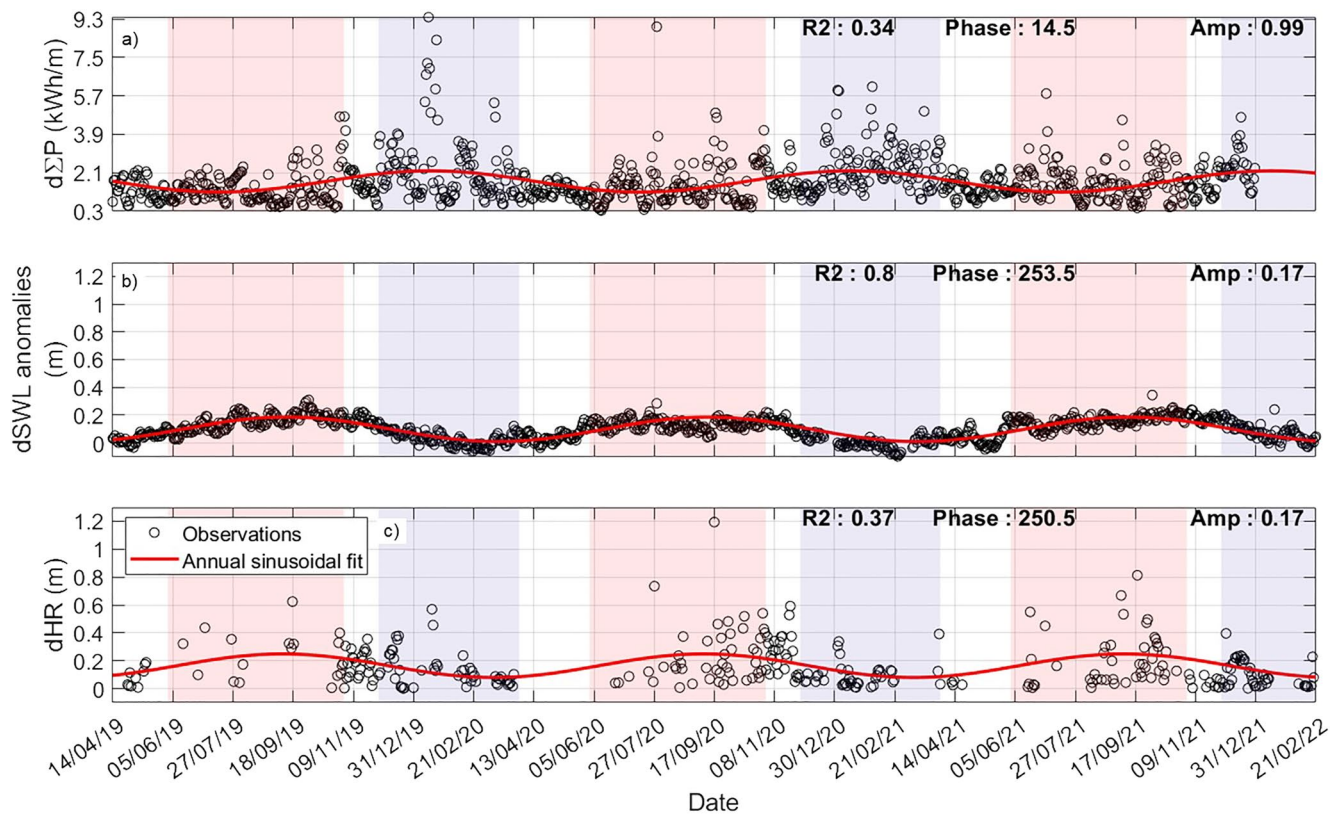


Figure 6. Data (black circles) and annual sinusoidal fit (red line) for daily cumulative wave power (a), still water level (SWL) anomalies (b), and daily highest runup (dHR) (c). For each plot, the Pearson correlation coefficient (R^2) between the data and the annual sinusoidal fit, the phase, and the amplitude (Amp) of the annual cycle is indicated. The cyclonic season is represented by a red background and the winter swell season by a blue background.

the offshore forcings associated, the position of RVL before the event, and the percentage of the difference between P1 and P2. All the events show a greater dHR on P2, but the difference between the two profiles varies. Event 3 shows the maximum runup values for P1 and P2 as 1.01 and 1.14 m, respectively. Event 4 has the greater difference between the two profiles, with a value of 0.21 m (42.8%) less on P2. Events 2 and 5 present a slight difference between the two profiles with values 0.05 m (7.7%) and 0.04 m (14.6%), respectively. Events 1 and

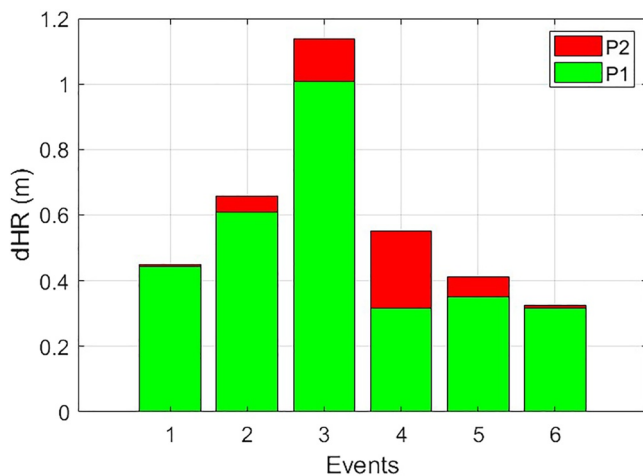


Figure 7. Daily highest runup (dHR) observed on P1 and P2 profiles for events when the vegetation limit is overreached.

6, with a dHR slightly exceeding the RVL, do not demonstrate a significant difference between the profiles (<0.01 m on each). Regarding concomitant offshore conditions, every event except 1 and 5 is associated with a high dSWL value (>0.4 m). But events 1 and 5 are associated with strong incident waves ($H_s = 3.82$ and 4.47 m and $T_p = 15.15$ and 11.11 s, respectively). Furthermore, a greater difference between the profiles is noted for greater runup events (i.e., events 2, 3, and 4) with dHR largely exceeding RVL, suggesting that the larger the excursion is in the vegetated area, the larger is the attenuation. The limited number of events reduces the rigor of further analysis. Thus, correlations with the offshore hydrodynamics and the dHR are not significant (p -values >0.05).

These observations suggest a stronger attenuation when dHR largely exceeds the RVL. The variability of RVL through time can also play a significant role. During event 4, the RVL was low, and the dHR difference between the two profiles was the greatest measured, suggesting that swash had been highly reduced by the vegetation. More energetic conditions, like event 2, with a higher RVL, have very small differences between P1 and P2, suggesting a possible retreat of the vegetation during the event, preventing any attenuation

Table 3

Parameters Associated With Total Water Level Events Exceeding the Vegetation Limit Where the Darker Coloring Indicates the Higher Data Values

Date	Offshore forcing			dHR (m)			RVL (m)	Attenuation %
	H_s (m)	T_p (s)	D_p (°)	SWL (m)	P1	P2		
1 01/19/2020	3.82	15.15	357.00	0.27	0.44	0.45	0.44	1.7
2 07/29/2020	4.63	11.11	76.00	0.41	0.61	0.66	0.50	7.7
3 09/18/2020	2.95	13.33	47.00	0.41	1.01	1.14	0.57	11.2
4 06/20/2021	2.36	9.26	86.00	0.34	0.32	0.55	0.34	42.8
5 07/03/2021	4.47	11.11	105.00	0.29	0.35	0.41	0.38	14.6
6 08/23/2021	2.71	8.55	74.00	0.45	0.32	0.32	0.25	2.2

in the swash excursion. Indeed, a vegetation retreat was observed on 29 September 2020, associated with event 2 (Figures 3c and 3d). This was also observed during event 6, when a regression of the vegetation was observed and lasted over 1 month.

3.2. In Situ Wave Observations

3.2.1. Wave Data Analysis

The data from field measurements were used to identify processes involved in nearshore hydrodynamic transformation by the reef and the resulting runup. Figure 7 presents the time series of the campaign, including offshore conditions.

The compilation of offshore wave conditions and the dHR is presented in Table 4. Three events exceeded $H_{s,95\%}$ (~2 m): events A, B, and C. The maximum H_s was reached on 06 September (event B) with a value of 2.8 m and a T_p of 13.7 s. These three events remained moderate in intensity and were related to cyclonic activity in the Atlantic basin relatively far from the study site. Additionally, the vegetation limit was not exceeded by the dHR during these events. Spectral time series on the FR, RC, and RF sensors (from offshore to the beach cf. Figure 1b) indicate that the FR sensor signals are mostly composed of SW band waves, while the RF contains more IG and VLF (Figures 8c–8e). The RC sensor lies in between the two other sensors. Furthermore, the RF time series shows alternating periods of a quasi-null spectrum (particularly at low tide) and periods of better swell penetration. This alternation is not visible in the other sensors' time series.

Compiling the data from all three sensors, the evolution of the mean H_{rms} from the FR to the RF illustrated the specific behavior of each frequency band while propagating toward the shore (Figure 9a). A clear attenuation of the SW band appears when comparing the FR and the RF sensors. The IG band shows a maximum at the RC position and then a slight attenuation on the RF; and the VLF band shows progressive amplification from offshore to the RF. The mean spectra for the three sensors on the cross-shore profile (Figure 9b) confirms this progressive attenuation of energy in the sea-swell band and the amplification to the lower bands.

3.2.2. RF Hydrodynamics

In order to evaluate the implication of different components on the dTWL, the results from the RF sensor to the concomitant values of the dTWL were compared. The RF sensor by its position close to the shoreline is expected to show a composition similar to the dTWL. In Figure 10, it is evident that most high dTWL values observed by the camera (Figure 10a) are linked to significant agitation measured on the RF (Figure 10b). Example of this pattern can be observed from 05 to 09 September (event B), on 20 September (unidentified as an event as H_s did not reach $H_{s,95\%}$), and at the very end of September (event C).

The linear correlation between the dTWL and the components of TWL measured on the RF (Figure 11) indicates the respective roles of the waves in

Table 4

Most Agitated Periods Parameters of the Measurement Campaign Where the Darker Coloring Indicates the Higher Data Values and “nd” Means No data

Event id	Peak date	Duration (days)	ΣP (kWh/m)	Peak conditions			dHR (m)	
				H_s (m)	T_p (s)	D_p (°)	P1	P2
A	08/28/2021	2.8	4.9	2.2	8.3	84	nd	0.3
B	09/06/2021	7.6	17.1	2.8	13.7	85	0.6	0.6
C	10/02/2021	3.5	8.2	2.4	11.6	60	0.6	0.6

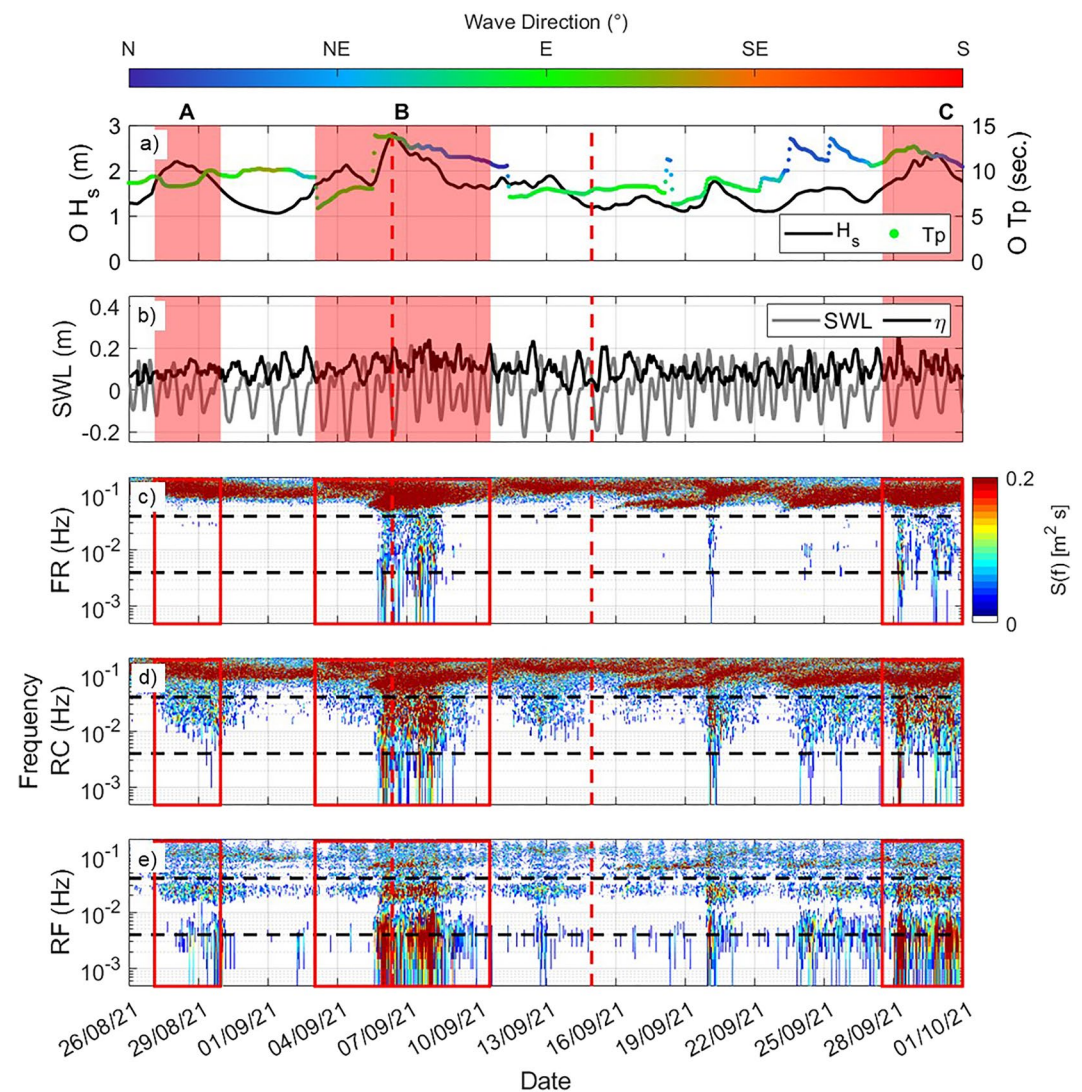


Figure 8. Hydrodynamic conditions for the wave measurement campaign. (a) Offshore H_s (referred as $O H_s$), T_p , and D_p from the MARC model, (b) still water level (SWL) measured at Pointe-à-Pitre tide gauge and setup on the reef flat (η), wave spectrum time series for (c) front reef (FR), (d) reef crest (RC), and (e) reef flat (RF). Horizontal dotted black lines represent the limits between infragravity (IG) wave and short waves (SW) and IG and very low frequency (VLF) wave. The Y-axis on (c), (d), and (e) is on a log scale. Events exceeding $H_{s\ 95\%}$ are highlighted by a red background (a and b) or identified by a red rectangle (c–e). Spectra extraction period for Figure 14 are marked by vertical red dotted line on each plot.

different spectral bands, setup and offshore water level. The SW band presents the most important contribution to the dTWL with a mean H_{rms} of 0.16 m; in second place, the setup represents a mean of 0.11 m. The SW and VLF waves slowly increase with dTWL, whereas setup remains quite stable. In contrast, the IG band presents a lower mean (0.06 m) but is better correlated with dTWL than other parameters ($R^2 = 0.46$). Thus, the relative contribution of the IG waves increases with dTWL leading to a low frequency (IG + VLF) contribution of the same order of magnitude as SW and setup for the highest dTWL.

In summary, these results suggest (a) a stronger contribution in the SW waves and setup on the dTWL but with (b) an increase in the IG contribution with dTWL.

3.2.3. Offshore Conditions Control on the RF Hydrodynamic

As the wave agitation measured in the RF depends on the reef-induced wave transformation, comparisons of wave agitation on the RF with the offshore data were performed (Figure 12). The comparison with the offshore wave's D_p is insignificant. However, the wave agitation on the RF for each frequency band is well correlated with the

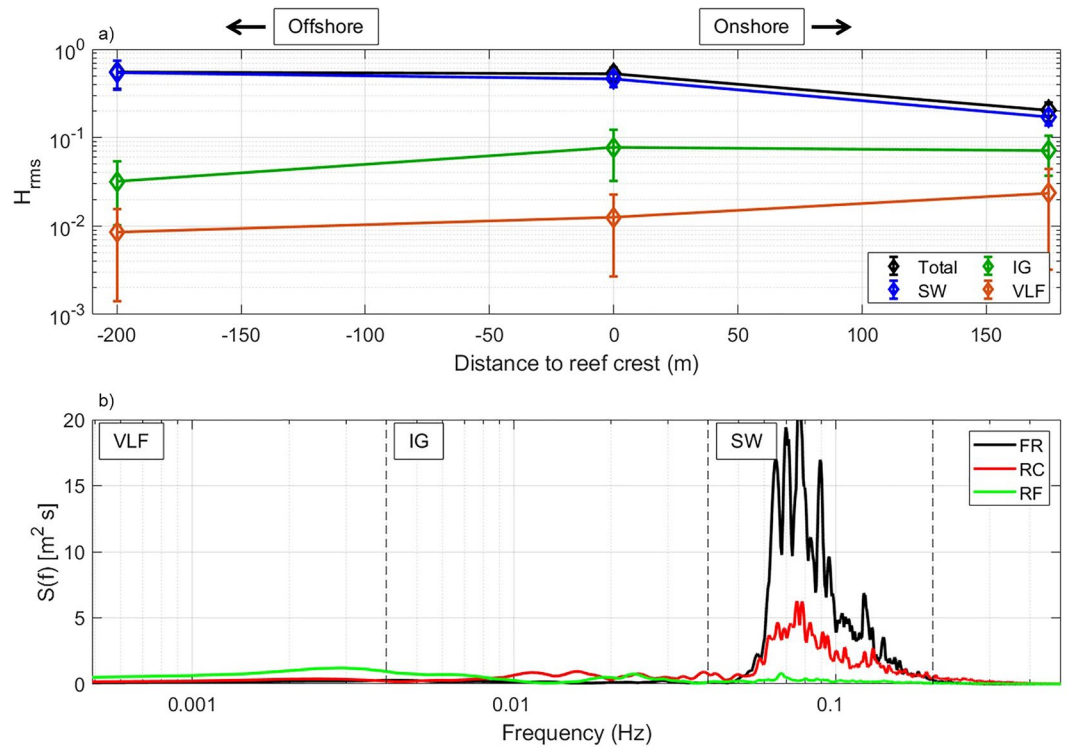


Figure 9. (a) Mean H_{rms} (diamonds) and H_{rms} standard deviation (error bars) per sensor. Short waves (SW) band observations are plotted in blue, infragravity (IG) band in green, and very low frequency (VLF) band in brown. (b) Maximum wave spectra of each sensor. To facilitate observations on the low frequencies, the Y-axis on (a) and the X-axis on (b) are on a log scale.

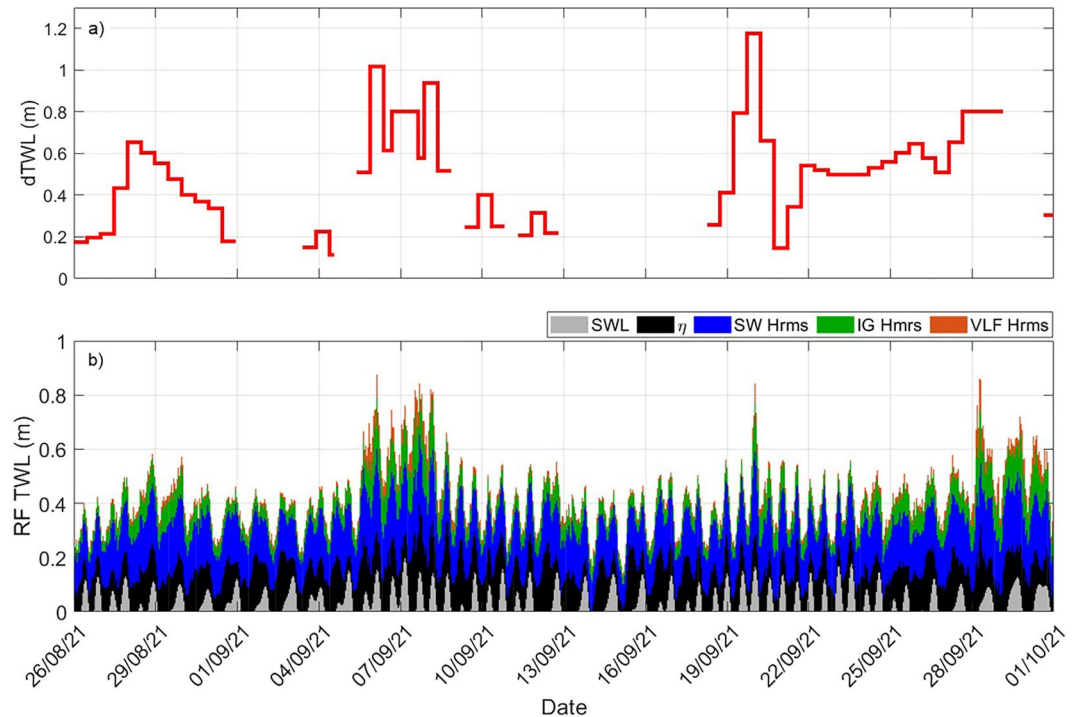


Figure 10. (a) Daily total water level (dTWL) evolution observed on camera during the hydrodynamic campaign, (b) TWL components extracted from the reef flat (RF) sensors.

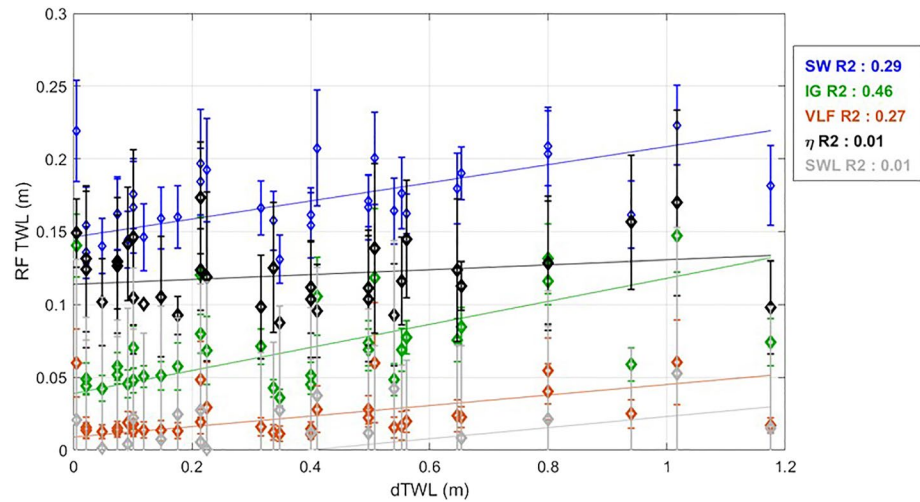


Figure 11. Linear regression of the daily total water level (dTWL) extracted from the camera and TWL components from the reef flat (RF) sensor. Diamonds represent the mean daily value and error bars, the standard deviation.

incident waves (R^2 ranging from 0.37 to 0.69 for H_s and T_p). Additionally, the trend on the IG band is stronger than on the other bands. As a consequence, the relative contribution of the IG band is higher for the most intense offshore conditions. Furthermore, the SWL versus the H_{rms} on the RF shows a significant correlation for the SW band only ($R^2 = 0.6$). Thus, high values of SWL are associated with a stronger penetration of the energy in the SW band and a lower transformation to low-frequency bands.

The wave transformation through the reef was further analyzed by comparing FR and RF measurements on each frequency band and the wave setup (Figure 13). Unlike the offshore wave data from the MARC model, the data from the FR sensor provides information on the whole wave spectra. Therefore, a comparison between the waves that have undergone minimal transformation from the FR sensor and the remaining waves from the RF may be completed for each frequency band. The transformation of each parameter (i.e., SW, IG, VLF, and setup) induced by the passage through the reef is illustrated in Figure 13.

The FR wave power shows a better correlation with RF parameters for the lower frequency bands ($R^2 = 0.84$ and 0.8 for IG and VLF, respectively) than with the SW frequency band ($R^2 = 0.6$), although the latter presents the highest value in general (Figure 13a). Nevertheless, for most intense incident conditions, the IG waves may reach the same height as the SW band (up to 0.15 m) (Figure 13b) and VLF waves may reach up to 0.1 m in height (Figure 13c).

The SWL has a clear effect on the penetration of SW; the H_{rms} at the RF sensor was about half the value for low SWL conditions. The effect of the SWL on the IG propagation and amplification at the RF sensor is less clear; although a high SWL seems to be associated with the highest IG component. No trend was observed for the VLF component.

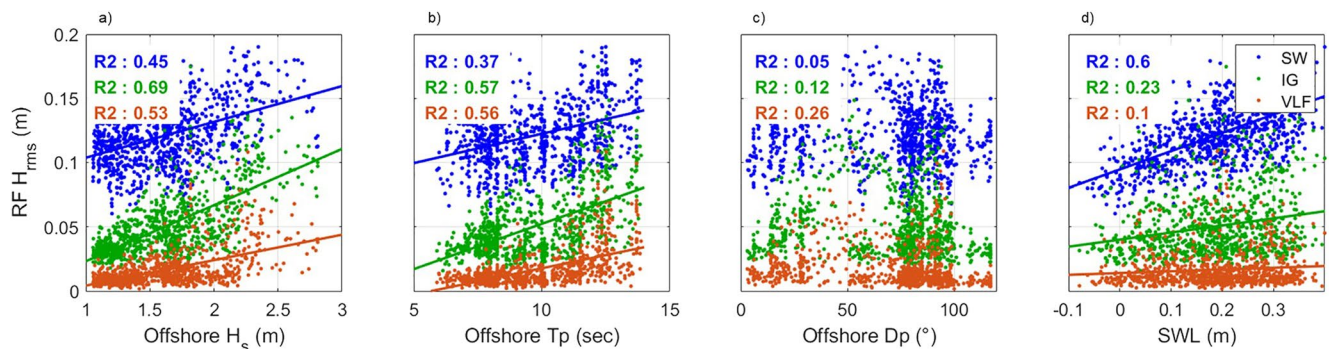


Figure 12. Linear regressions of H_{rms} measured by the reef flat (RF) sensor against offshore wave parameters (a) H_s , (b) T_p , (c) D_p , and (d) still water level (SWL) measured at Pointe-à-Pitre tide gauge.

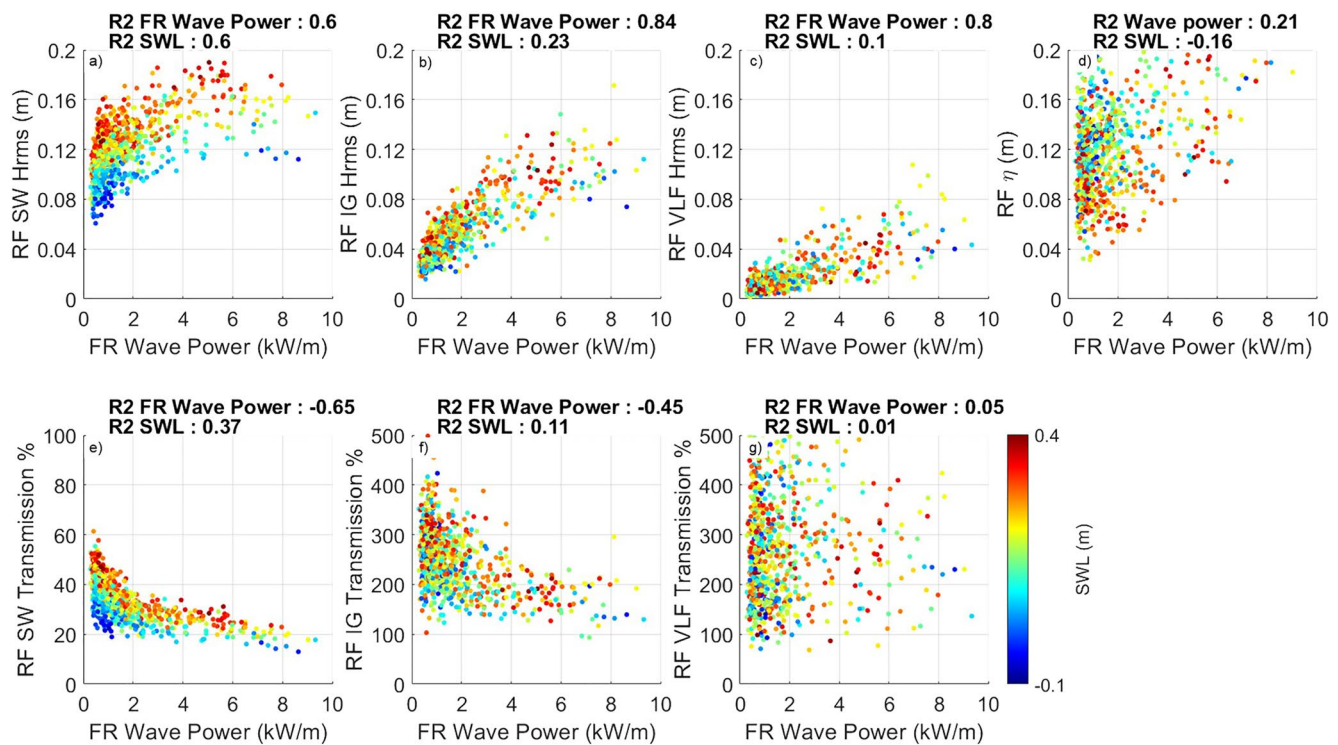


Figure 13. Upper row presents (a) short waves (SW), (b) infragravity (IG), (c) very low frequency (VLF) H_{rms} , and (d) setup “ η ” against the reef flat (RF) sensor wave power. The lower row presents wave transmission between front reef (FR) and RF sensors against RF sensor wave power for (e) the SW, (f) the IG, and, (g) the VLF band. The point's color represents sea-level variations.

Strong wave conditions during low SWL correspond to a predominance of low-frequency components in the H_{rms} at the RF sensor. The setup on the RF is uncorrelated with the wave power and the SWL, even though it seems to be greater for low offshore wave power associated with a low SWL (i.e., no tendency for higher wave energy conditions). The setup exhibits significant values ranging from 0.04 to 0.2 m (Figure 13d).

Wave transmission over the reef is estimated by comparing spectral components on the FR and on the RF (Figures 13e–13g). SW is attenuated for every condition with a transmission ranging from 15% for the most intense wave power to 60% during calm periods associated with high sea levels. The SW shows a good inverse correlation with the wave power ($R^2 = -0.65$) and a mild correlation with the SWL ($R^2 = 0.37$). This suggests a better shortwave conservation for smaller incident conditions and high sea levels. When the SWL is low, and for all incident wave conditions, the attenuation of wave energy by the reef is greater than 70% (i.e., transmission does not exceed 30%). The IG and the VLF waves are almost always amplified with values ranging, respectively, from 100% to 500% and from 75% to 500%. Even though every condition engenders an IG wave band amplification, the wave transmission decreases with increasing wave power ($R^2 = -0.45$). The correlation with the SWL and IG wave transmissions is insignificant ($R^2 = 0.11$). The VLF waves transmission does not appear to be correlated with either the wave power or the SWL.

In summary, these results indicate (a) a strong correlation between incident waves and waves on the RF at all frequency bands but not with the setup; (b) an increasing contribution of lower frequency bands with increasing wave power; (c) a strong attenuation of the SW exceeding 80% for low SWL; and (d) a decreasing transmission on the SW and the IG bands for increasing wave power probably resulting from wave transformation occurring on the FR during the most energetic conditions.

4. Discussion

In this study, a continuous multiyear runup time series obtained from video monitoring was used along with offshore wave data sets and local hydrodynamic measurements in a fringing reef system. This allowed further

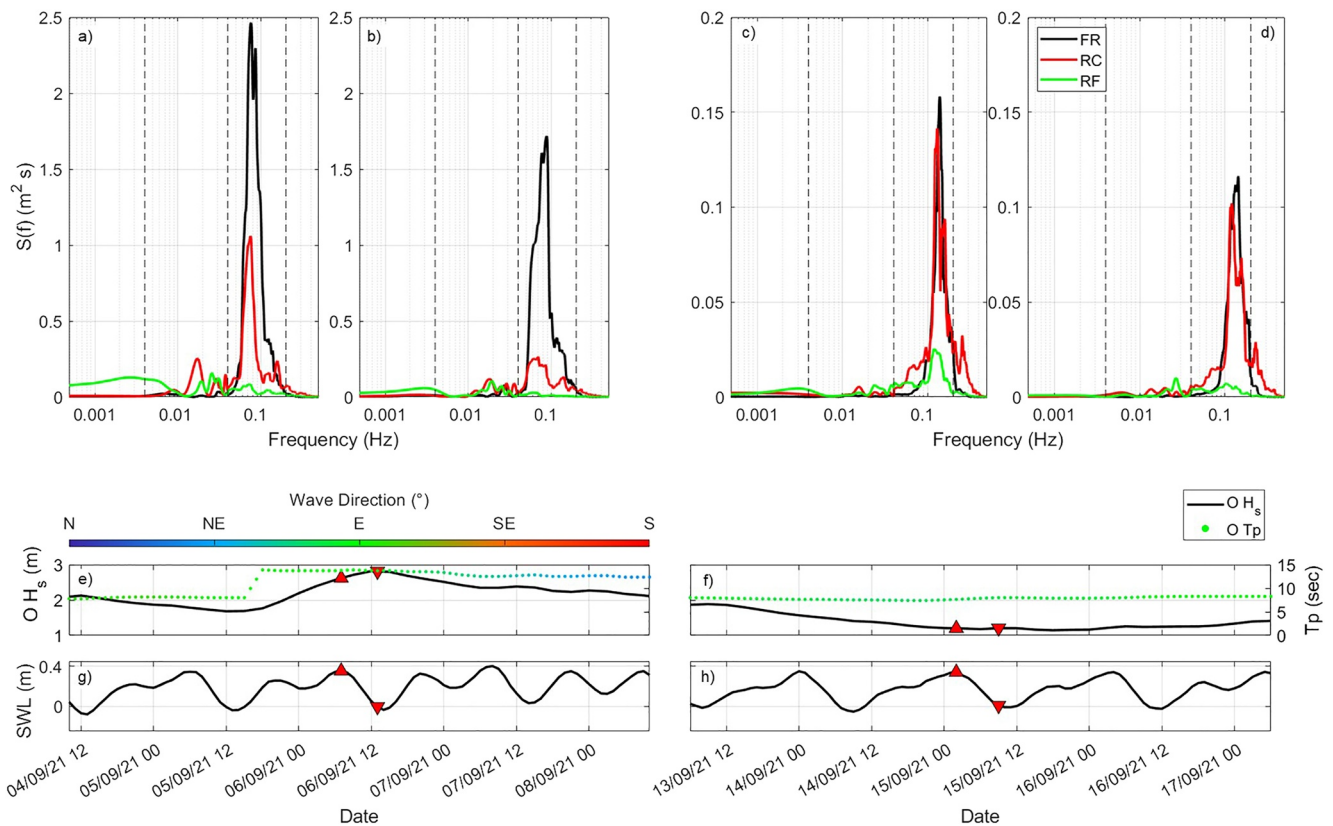


Figure 14. Energy spectra at front reef (FR; black line), reef crest (RC; red line), and reef flat (RF) position (green line) corresponding to storm conditions on 06 September at high (a) and low (b) tides and calm conditions on 15 September at high (c) and low (d) tides. Offshore wave conditions (e) and (f) and sea-level variations (g) and (h) are plotted under spectral graphs for both periods. The period of the extracted bursts is represented by an upward red triangle for high tide and a downward red triangle for low tide.

analyses, at different times and spatial scales, of the key processes and parameters involved in the control of the runup.

Overall, pluriannual observations indicate (a) a control of the dHR by the dSWL anomalies both showing a strong and similar annual cyclicality, (b) significantly lower dHR values on the profile with vegetation which is particularly noticeable when an important vegetation length is crossed (e.g., low RVL and/or high dHR), and (c) a retroactive control of the dHR on vegetation position.

4.1. Reef Control on Runup

Coral reef wave filtering by wave breaking and bottom friction depends on the water depth above the reef (Becker et al., 2014; Sous et al., 2019; Yao et al., 2012). Hence, low water depth on the reef induces high filtering of the swell, while high water depth induces a lower filtering and greater wave energy potentially reaching the beach. Such a phenomenon was also observed on sandy beaches with sedimentary or rocky structures like bars (e.g., Guedes et al., 2011) but it is amplified in the presence of a coral reef because of the steepness, the potentially wide width of the coral platform, the high structural complexity, and the crest shallowness of such an environment.

The data analysis on the pluriannual daily time series corroborates this conventional assumption, by showing a strong correlation between dHR and dSWL rather than incident wave energy. The relative implication of the dSWL components (astronomical tides and anomalies) was also estimated. A good correlation was found with the anomalies but not with the tide component. At the daily frequency, this latter corresponds to neap to spring tides cycles, which have a limited range (~0.1 m). Conversely, the anomalies exhibit a greater range (~0.4 m). Therefore, since the range of variations of dSWL anomalies is four times greater than the daily tide variations, this could explain the stronger correlation with anomalies. Additionally, a strong annual cyclicality was identified on the dSWL anomalies data set with a phase and amplitude similar to the dHR observations. The annual cyclicality

extracted on dSWL corroborates previous research on the seasonal sea-level cycle in the Caribbean (Torres & Tsimplis, 2012). This work also concludes that this cyclicity is the result of seasonal changes in the steric expansion of water bodies. The amplitude of the annual cycle on the dHR is the same as for dSWL (~ 0.17 m). Yet, the vast majority of runup events occurred during the highest portion of the cycle (i.e., at the peak identified in mid-September). In contrast, several strong wave events occurred during the lower portion of the cycle but did not generate high dHR. These elements allow us to conclude that the steric seasonal cycle acts as a strong control on runup by varying the depth over the reef and thus affecting the wave attenuation by the reef structure. The attenuation potential generally increases during the low portion of the cycle from December to May, and is less efficient during the highest portion of the cycle from June to November. Even though the seasonality of steric expansion in the Caribbean and Guadeloupe Island in particular has already been identified, the link with runup in a reef context had never been highlighted. Moreover, as a greater portion of incident energy reaches the shoreline level during the high portion of the annual cycle, it may impact beach morphology. In other words, this annual variation may be responsible for seasonal shoreline and beach morphological evolution in association with wave forcing. This corroborates other shoreline observations from video monitoring on other reef-lined beaches in Guadeloupe (Moisan et al., 2021).

4.2. Wave Transformation on the Reef

Pluriannual observations using a camera underscored the processes involved in the seasonal time scales. On-site measurements of hydrodynamics permitted the ability to (a) address processes at a finer time scale, (b) extract the different components of agitation on the RF and to evaluate their respective effects, and (c) provide insights on the control by different processes involved in the observed dHR.

In a meta-analysis of over 255 studies (Ferrario et al., 2014), established that a mean of 84% of the wave is attenuated by coral reef systems. The comparison between fore reef and RF measurements at Anse Maurice indicated an overall mean attenuation of 65% on wave height with SWL and wave intensity dependency. This mild attenuation may be the consequence of the particularly chaotic and slashed composition and the limited width of this fringing reef system.

The spectral analysis of wave data provides further information on the attenuation.

Indeed, only the SW that represent the vast majority of offshore wave energy spectra are subject to attenuation. IG waves show a maximum on the RC followed by a slight attenuation on the RF sensors (Figures 8 and 9). The VLF waves increase gradually from the FR to the RF. This behavior reflects the transformation of a fraction of the SW when dissipated into IG waves, and then a transformation of IG into VLF waves on the RF. Thus, IG and VLF waves of up to 0.2 and 0.1 m, respectively, are observed on the RF, whereas these low-frequency undulations were almost insignificant before reaching the reef level (Figures 8 and 9). This result indicates that most IG and VLF are generated by breakpoint forcing (Symonds et al., 1982) and a minor fraction comes from incident-bound long waves (Longuet-Higgins & Stewart, 1964), as it was observed by several authors (e.g., Cheriton et al., 2016; Masselink et al., 2019; Péquignot et al., 2009; Pomeroy et al., 2012).

A sea-level dependency is exhibited because stronger attenuation of the SW was measured during low sea levels than during high sea levels (Figure 13e). Contrary to the daily observations, high-frequency tide variations appear on sensors data sets and constitute the main parameter controlling SWL variations (with a range of 0.4 m for the data collection period). Thus, low-frequency waves have the greatest relative contribution to RF hydrodynamics for the most intense incident waves and low water levels. It is worthwhile to remember that the hydrodynamic conditions observed during the measurement campaign are moderate with regard to the entire data set. Therefore, following on from this consideration, IG waves could represent the main contribution during more intense conditions.

Furthermore, even though all components of runup, besides the setup, depend on the incident wave power, the transmission is inversely proportional to the wave power in the SW and the IG bands. This indicates that for higher incident energy, a further portion of SW is dissipated on the forereef and RC even if the observed resulting agitation on the RF is stronger than for calm conditions. IG transmission is also inversely correlated with incident wave power and VLF transmission did not show a significant correlation. It has been assumed that for the most intense conditions, a portion of the incident SW has already been transformed at the FR position (~ 8 m in depth). Significant IG motions on the FR are then identified (see events A, B, and C in Figure 8c), biasing the

transmission calculation, which thus shows lower values. Note that even if the setup showed significant values up to 0.2 m, it was poorly correlated with the wave power and the SWL.

The waves' spectral transformation during a storm at high (a) and low (b) tides and during a calm period also at high (c) and low (d) tides is presented in Figure 14. The energy switch from the SW band to the IG/VLF band is particularly important at high tide (Figures 14a and 14c) and less obvious at low tide (Figures 14b and 14d). Furthermore, the amplification of the IG waves on the RC is followed by amplification on the late IG/early VLF band on the RF, particularly during agitated conditions (Figures 14a and 14b). For calm conditions (Figures 14c and 14d), the transformation is less marked and only visible between the RC and the RF as smaller waves may penetrate further into the reef system before shoaling and breaking. Moreover, the energy peak in the VLF band for agitated conditions reaches the same order of magnitude as the peak in the IG band, when the SW band is less important (in particular during low tide). This strengthens the hypothesis stating that most of the agitation on the RF is gathered by low-frequency undulation during storm conditions.

4.3. Hydrodynamic Control on Vegetation Limit

This data set on dHR, collected over 2 years and 10 months, permitted the identification of six events exceeding the upper beach vegetation limit. The number of observations is not sufficient to properly conclude the direct effect on runup; however, worthwhile insights can be gleaned.

First, all events exceeding vegetation limits showed greater runup on the profile P2 which is without vegetation. Moreover, it was noted that events crossing the larger distance of vegetation exhibited a greater difference between the two profiles which supports the role of vegetation on runup dampening. The maximum runup difference between profiles is 42.8% or 0.26 m and the mean for the six events is 13.4% or 0.08 m.

Second, the cyclicity of the vegetation limit was evaluated; it was found that the vegetation limit reacts to agitation retroactively. Indeed, two occurrences were observed that resulted in severe setbacks: following an important runup event exceeding the vegetation limit and during a period including several events just reaching the vegetation. This appeared as a magnitude change of the vegetation limit of ~ 0.6 m each time. However, most events just reaching the limit or not exceeding it largely did not affect the vegetation limit.

We looked at RVL, which depends on SWL and vegetation evolution and it was observed that vegetation only moves backward when it reaches a critical level of 0.2 m, meaning that a runup of only 0.2 m may reach the vegetation. Each time the vegetation achieved this limit, it engendered a quick and strong retreat of ~ 0.5 m in magnitude on the profile. Two hypotheses are advanced to explain this dynamic. First, the front layer of vegetation (developing lower on the beach profile) evolves quickly and may consequently have lower leaf, stem, and root densities than the vegetation a few meters back (although the vegetation species are the same at this scale). Second, the low front layer vegetation is exposed to less dissipated swash with possibly a thicker swash lens. Both hypotheses could explain why, high runup event with RVL above 0.6 m did not generate a degradation of vegetation (see event 3 in Figures 3 and 7). Such declines in vegetation were observed in 2020 and 2021 in parallel with the annual peak of the SWL. It was not observed in 2019, probably because the vegetation limit was higher due to human mechanical destruction.

5. Conclusions

Using 2 years and 10 months video monitoring of wave runup, as well as measurements of wave dynamics on the fringing coral reef of Anse Maurice in Guadeloupe Island, we analyzed processes involved in swash inundation from event scale to seasonal scale.

As it was already described in the literature, it was observed that:

- The IG and VLF wave bands amplify along the reef platform leading to low-frequency dominance on the RF in particular for the most energetic conditions.
- At short time scale, the tide controls SW transmission on the RF with more filtering at low tide.

This study evidenced new processes influencing TWL and subsequent inundation. Particularly it was observed that:

- The annual cycle on steric expansion has a significant effect on the SWL and thus on the depth over the reef, wave attenuation on the RC, and the dHR. Even if the amplitude of this annual cyclicity is limited (0.17 m) it

presents a strong control on the dHR, shown as periods with further wave filtering (in terms of frequency and intensity) and periods with less wave filtering at the scale of the year. Thus, the same incident wave condition may have a very different impact simply based on its time of occurrence.

- The presence of upper beach vegetation was found to induce a difference in runup during storms, and the vegetation limit demonstrated a strong seasonality in response to runup fluctuations.

More research is needed to investigate the role of this ecosystem in reducing wave runup and thus coastal inundation, particularly during more extreme events. In a climate change context with sea-level rise and a likely increase in extreme events, the higher submergence of reefs will induce an increase in runup and coastal flooding events in reef coast environments. This multiyear time series of daily maximum runups provide new insight on runup control by annual variations in the sea level, as well as, by processes involved at a finer scale. Further work in this study will involve a numerical experiment to be conducted to investigate the processes during more intense storms than those observed during the study period.

Data Availability Statement

The daily total water levels and vegetation limit heights on two cross-shore profiles that were acquired and analyzed in the framework of this manuscript are freely available via <https://doi.org/10.5281/zenodo.7662638> with Creative Commons Attribution 4.0 International license (Laignre et al., 2023).

Acknowledgments

The study takes part of a PhD thesis work funded by the BRGM within the EU Interreg Caribbean CARIB-COAST project (Grant 4907). Offshore wave conditions extracted from the MARC model were provided by the IFREMER. Tide gauge sea-level observations were provided by the SHOM. The authors also thank T. Delahaye, M. Norden and S. Chapron for their help in field experiments.

References

- Aarninkhof, S. G. J., & Ruessink, B. G. (2004). Video observations and model predictions of depth-induced wave dissipation. *IEEE Transactions on Geoscience and Remote Sensing*, 42(11), 2612–2622. <https://doi.org/10.1109/TGRS.2004.835349>
- Almar, R., Bonneton, P., Senechal, N., & Roelvink, D. (2008). Wave celerity from video imaging: A new method. *Coastal Engineering*, 661–673. https://doi.org/10.1142/9789814277426_0056
- Andriolo, U., Sánchez-García, E., & Tabora, R. (2019). Operational use of surfcam online streaming images for coastal morphodynamic studies. *Remote Sensing*, 11(1), 78. <https://doi.org/10.3390/rs11010078>
- Baldock, T. E. (2012). Dissipation of incident forced long waves in the surf zone—Implications for the concept of “bound” wave release at short wave breaking. *Coastal Engineering*, 60, 276–285. <https://doi.org/10.1016/j.coastaleng.2011.11.002>
- Becker, J. M., Merrifield, M. A., Ford, M., & Hoteit, I. (2014). Water level effects on breaking wave setup for Pacific Island fringing reefs. *Journal of Geophysical Research: Oceans*, 119, 3909–3925. <https://doi.org/10.1002/2013JC009563>
- Bergsma, E. W. J., & Almar, R. (2018). Video-based depth inversion techniques, a method comparison with synthetic cases. *Coastal Engineering*, 138, 199–209. <https://doi.org/10.1016/j.coastaleng.2018.04.025>
- Bindoff, N. L., Willebrand, J., Artale, V., Cazenave, A., Gregory, J., Gulev, S., et al. (2007). Observations: Oceanic climate change and sea level coordinating. In *Climate Change 2007: The Physical Science Basis. Contribution of Working Group I to the Fourth Assessment Report of the Intergovernmental Panel on Climate Change* (pp. 387–429). Retrieved from <https://eprints.soton.ac.uk/id/eprint/50391>
- Buckley, M. L., Lowe, R. J., Hansen, J. E., Van Dongeren, A. R., & Storlazzi, C. D. (2018). Mechanisms of wave-driven water level variability on reef-fringed coastlines. *Journal of Geophysical Research: Oceans*, 123, 3811–3831. <https://doi.org/10.1029/2018JC013933>
- Castelle, B., Marieu, V., Bujan, S., Splinter, K. D., Robinet, A., Sénéchal, N., & Ferreira, S. (2015). Impact of the winter 2013–2014 series of severe Western Europe storms on a double-barred sandy coast: Beach and dune erosion and megacusp embayments. *Geomorphology*, 238, 135–148. <https://doi.org/10.1016/j.geomorph.2015.03.006>
- CEREMA. (2021). Fiches synthétiques de mesure des états de mer-Tome 3-Outre-mer.
- Charles, E., Idier, D., Delecluse, P., Déqué, M., & Le Cozannet, G. (2012). Climate change impact on waves in the Bay of Biscay, France. *Ocean Dynamics*, 62(6), 831–848. <https://doi.org/10.1007/s10236-012-0534-8>
- Chelton, D. B., & Enfield, D. B. (1986). Ocean signals in tide gauge records. *Journal of Geophysical Research*, 91(B9), 9081–9098. <https://doi.org/10.1029/JB091iB09p09081>
- Chelton, D. B., Schlax, M. G., Samelson, R. M., & De Zoete, R. A. (2007). Global observations of large oceanic eddies. *Geophysical Research Letters*, 34, L15606. <https://doi.org/10.1029/2007GL030812>
- Cheriton, O., Storlazzi, C. D., & Rosenberger, K. J. (2016). Observations of wave transformation over a fringing coral reef and the importance of low-frequency waves and offshore water levels to runup, overwash, and coastal flooding. *Journal of Geophysical Research: Oceans*, 121, 3121–3140. <https://doi.org/10.1002/2015JC011231>
- Cheriton, O., Storlazzi, C. D., & Rosenberger, K. J. (2020). In situ observations of wave transformation and infragravity bore development across reef flats of varying geomorphology. *Frontiers in Marine Science*, 7, 351. <https://doi.org/10.3389/fmars.2020.00351>
- Church, J. A. (2015). Sea-level science: Understanding tides, surges, tsunamis and mean sea-level changes. *Oceanography*, 28(1), 177–178. <https://doi.org/10.5670/oceanog.2015.24>
- Costa, M. B. S. F., Araújo, M., Araújo, T. C. M., & Siegle, E. (2016). Influence of reef geometry on wave attenuation on a Brazilian coral reef. *Geomorphology*, 253, 318–327. <https://doi.org/10.1016/j.geomorph.2015.11.001>
- Egbert, G. D., Bennett, A. F., & Foreman, M. G. G. (1994). TOPEX/POSEIDON tides estimated using a global inverse model. *Journal of Geophysical Research*, 99(C12), 24821–24852. <https://doi.org/10.1029/94JC01894>
- Ellison, J. C. (2018). Pacific island beaches: Values, threats and rehabilitation. In C. M. Botero, O. Cervantes, & C. W. Finkl (Eds.), *Beach management tools—Concepts, methodologies and case studies* (pp. 679–700). Springer International Publishing. https://doi.org/10.1007/978-3-319-58304-4_34
- Enfield, D. B., & Allen, J. S. (1980). On the structure and dynamics of monthly mean sea level anomalies along the Pacific coast of north and south America. *Journal of Physical Oceanography*, 10(4), 557–578. [https://doi.org/10.1175/1520-0485\(1980\)010<0557:OTSADO>2.0.CO;2](https://doi.org/10.1175/1520-0485(1980)010<0557:OTSADO>2.0.CO;2)

- Escudero, M., Mendoza, E., & Silva, R. (2020). From nature-based to ecologically enhanced beach protection strategies: An experimental comparison (pp. 981–988). https://doi.org/10.18451/978-3-939230-64-9_098
- Ferrario, F., Beck, M. W., Storlazzi, C. D., Micheli, F., Shepard, C. C., & Airolidi, L. (2014). The effectiveness of coral reefs for coastal hazard risk reduction and adaptation. *Nature Communications*, 5, 3794. <https://doi.org/10.1038/ncomms4794>
- Fisher, R. A. (1958). Statistical methods for research workers (13th ed.). In S. Kotz, & N. L. Johnson (Eds.), *Breakthroughs in Statistics*. Springer. https://doi.org/10.1007/978-1-4612-4380-9_6
- Ford, M. R., Becker, J. M., & Merrifield, M. A. (2013). Reef flat wave processes and excavation pits: Observations and implications for Majuro atoll, Marshall Islands. *Journal of Coastal Research*, 288, 545–554. <https://doi.org/10.2307/23486338>
- Gerritsen, F. (1980). Wave attenuation and wave set-up on a coastal reef. In Coastal engineering proceedings (pp. 444–461). <https://doi.org/10.1061/9780872622647.028>
- Gill, A. E., & Niller, P. P. (1973). The theory of the seasonal variability in the ocean. *Deep Sea Research and Oceanographic Abstracts*, 20(2), 141–177. [https://doi.org/10.1016/0011-7471\(73\)90049-1](https://doi.org/10.1016/0011-7471(73)90049-1)
- Greene, C. A., Thirumalai, K., Kearney, K. A., Delgado, J. M., Schwanghart, W., Wolfenbarger, N. S., et al. (2019). The climate data toolbox for MATLAB. *Geochemistry, Geophysics, Geosystems*, 20, 3774–3781. <https://doi.org/10.1029/2019GC008392>
- Guedes, R. M. C., Bryan, K. R., Coco, G., & Holman, R. A. (2011). The effects of tides on swash statistics on an intermediate beach. *Journal of Geophysical Research*, 116, C04008. <https://doi.org/10.1029/2010JC006660>
- Guillen, L., Pallardy, M., Legendre, Y., Torre, Y., & Loireau, C. (2017). Morphodynamique du littoral Guadeloupéen. Phase 1: Définition et mise en place d'un réseau d'observation et de suivi du trait de côte: Evaluation historique du trait de côte Guadeloupéen. Rapport final: Vol. M (Issue RP-66653-FR, p. 21109).
- Harris, D. L., Rovere, A., Casella, E., Power, H., Canavesio, R., Collin, A., et al. (2018). Coral reef structural complexity provides important coastal protection from waves under rising sea levels. *Science Advances*, 4(2), eaao4350. <https://doi.org/10.1126/sciadv.aao4350>
- Hawkins, T. W., Gourirand, I., Allen, T., & Belmadani, A. (2022). Atmospheric drivers of oceanic north swells in the eastern Caribbean. *Journal of Marine Science and Engineering*, 10(2), 183. <https://doi.org/10.3390/jmse10020183>
- Holland, K. T., Holman, R. A., Lippmann, T. C., Stanley, J., & Plant, N. (1997). Practical use of video imagery in nearshore oceanographic field studies. *IEEE Journal of Oceanic Engineering*, 22(1), 81–92. <https://doi.org/10.1109/48.557542>
- Holman, R. A., & Stanley, J. (2007). The history and technical capabilities of Argus. *Coastal Engineering*, 54(6), 477–491. <https://doi.org/10.1016/j.coastaleng.2007.01.003>
- Johnston, E., & Ellison, J. C. (2014). Evaluation of beach rehabilitation success, turners beach, Tasmania. *Journal of Coastal Conservation*, 18(6), 617–629. <https://doi.org/10.1007/s11852-014-0334-z>
- Knutson, T., Camargo, S. J., Chan, J. C. L., Emanuel, K., Ho, C. H., Kossin, J., et al. (2019). Tropical cyclones and climate change assessment. Part II: Projected response to anthropogenic warming. *Bulletin of the American Meteorological Society*, 100(10), 1987–2007. <https://doi.org/10.1175/BAMS-D-18-0189.1>
- Krien, Y., Dudon, B., Roger, J., & Zahibo, N. (2015). Probabilistic hurricane-induced storm surge hazard assessment in Guadeloupe, Lesser Antilles. *Natural Hazards and Earth System Sciences Discussion*, 3, 401–427. <https://doi.org/10.5194/nhessd-3-401-2015>
- Laigre, T., Balouin, Y., Nicolae-Lerma, A., Moisan, M., Valentini, N., Villaroel-Lamb, D., & La Torre, Y. D. (2023). Seasonal and episodic runup variability on a Caribbean reef-lined beach [Dataset]. Zenodo. <https://doi.org/10.5281/zenodo.7662638>
- Longuet-Higgins, M. S., & Stewart, R. W. (1962). Radiation stress and mass transport in gravity waves, with application to 'surf beats'. *Journal of Fluid Mechanics*, 13(4), 481–504. <https://doi.org/10.1017/S0022112062000877>
- Longuet-Higgins, M. S., Stewart, R. W., & Chen, Q. (1964). Radiation stresses in water waves; a physical discussion, with applications. *IEEE Transactions on Industrial Electronics*, 60(9), 3775–3783. <https://doi.org/10.1109/TIE.2012.2208438>
- Lowe, R. J., Falter, J. L., Bandet, M. D., Pawlak, G., Atkinson, M. J., Monismith, S. G., & Koseff, J. R. (2005). Spectral wave dissipation over a barrier reef. *Journal of Geophysical Research*, 110, C04001. <https://doi.org/10.1029/2004JC002711>
- Lugo-Fernández, A., Roberts, H. H., & Suhayda, J. N. (1998). Wave transformations across a Caribbean fringing-barrier Coral Reef. *Continental Shelf Research*, 18(10), 1099–1124. [https://doi.org/10.1016/S0278-4343\(97\)00020-4](https://doi.org/10.1016/S0278-4343(97)00020-4)
- Mardia, K. V., & Jupp, P. E. (2000). Correlation and regression. In *Directional statistics*. John Wiley & Sons.
- Masselink, G., Castelle, B., Scott, T., Dodet, G., Suanes, S., Jackson, D., & Floc'h, F. (2016). Extreme wave activity during 2013/2014 winter and morphological impacts along the Atlantic coast of Europe. *Geophysical Research Letters*, 43, 2135–2143. <https://doi.org/10.1002/2015GL067492>
- Masselink, G., Tuck, M., McCall, R., van Dongeren, A., Ford, M., & Kench, P. (2019). Physical and numerical modeling of infragravity wave generation and transformation on coral reef platforms. *Journal of Geophysical Research: Oceans*, 124, 1410–1433. <https://doi.org/10.1029/2018JC014411>
- Melito, L., Parlagreco, L., Devoti, S., & Brocchini, M. (2022). Wave- and tide-induced infragravity dynamics at an intermediate-to-dissipative microtidal beach. *Journal of Geophysical Research: Oceans*, 127, e2021JC017980. <https://doi.org/10.1029/2021JC017980>
- Moisan, M., Delahaye, T., Laigre, T., & Valentini, N. (2021). Suivi des échouages de sargasses et de l'évolution du trait de côte par caméra autonome en Guadeloupe: Analyse des résultats et bilan des observations. Rapport final. In *BRGM/RP-712-FR*.
- NHC. (2021). Hurricane Teddy (AL202020). Retrieved from https://www.nhc.noaa.gov/data/tcr/AL202020_Teddy.pdf
- Nicolae Lerma, A., Pedreros, R., Robinet, A., & Sénéchal, N. (2017). Simulating wave setup and runup during storm conditions on a complex barred beach. *Coastal Engineering*, 123, 29–41. <https://doi.org/10.1016/j.coastaleng.2017.01.011>
- Ning, Y., Liu, W., Sun, Z., Zhao, X., & Zhang, Y. (2018). Parametric study of solitary wave propagation and runup over fringing reefs based on a Boussinesq wave model. *Journal of Marine Science and Technology*, 24(2), 512–525. <https://doi.org/10.1007/s00773-018-0571-1>
- Paquier, A.-É., Laigre, T., Belon, R., Balouin, Y., Valentini, N., & Mugica, J. (2020). Video monitoring of Posidonia oceanica banquettes on pocket beaches, Northern Corsica. In *XVIèmes Journées Nationales Génie Côtier-Génie Civil*. Retrieved from <https://hal.archives-ouvertes.fr/hal-02931679>
- Pearson, S. G., Storlazzi, C. D., Van Dongeren, A. R., Tissier, M. F. S., & Reniers, A. J. H. M. (2017). A Bayesian-based system to assess wave-driven flooding hazards on coral reef-lined coasts. 99–117. <https://doi.org/10.1002/2017JC013204>
- Péquignat, A. C. N., Becker, J. M., Merrifield, M. A., & Aucan, J. (2009). Forcing of resonant modes on a fringing reef during tropical storm Man-Yi. *Geophysical Research Letters*, 36, L03607. <https://doi.org/10.1029/2008GL036259>
- Plant, N. G., Aarninkhof, S. G. J., Turner, I. L., & Kingston, K. S. (2007). The performance of shoreline detection models applied to video imagery. *Journal of Coastal Research*, 23(3), 658–670. [https://doi.org/10.2112/1551-5036\(2007\)23\[658:TPOSDM\]2.0.CO;2](https://doi.org/10.2112/1551-5036(2007)23[658:TPOSDM]2.0.CO;2)
- Pomeroy, A., Lowe, R. J., Symonds, G., Dongeren, A. V., & Moore, C. (2012). The dynamics of infragravity wave transformation over a fringing reef. *Journal of Geophysical Research*, 117, C11022. <https://doi.org/10.1029/2012JC008310>
- Quataert, E. (2015). Wave runup on atoll reefs (MSc thesis) (p. 89).

- Quataert, E., Storlazzi, C., van Dongeren, A., & McCall, R. (2020). The importance of explicitly modelling sea-swell waves for runup on reef-lined coasts. *Coastal Engineering*, *160*, 103704. <https://doi.org/10.1016/j.coastaleng.2020.103704>
- Reguero, B. G., Méndez, F. J., & Losada, I. J. (2013). Variability of multivariate wave climate in Latin America and the Caribbean. *Global and Planetary Change*, *100*, 70–84. <https://doi.org/10.1016/j.gloplacha.2012.09.005>
- Rodriguez-padilla, I., Castelle, B., Marieu, V., Bonneton, P., Mouragues, A., Martins, K., & Morichon, D. (2021). Wave-filtered surf zone circulation under high-energy waves derived from video-based optical systems. *Remote Sensing*, *13*(10), 1874.
- Roeber, V., & Bricker, J. D. (2015). Destructive tsunami-like wave generated by surf beat over a coral reef during Typhoon Haiyan. *Nature Communications*, *6*(1), 7854. <https://doi.org/10.1038/ncomms8854>
- Rueda, A., Cagigal, L., Pearson, S., Antolínez, J. A. A., Storlazzi, C., van Dongeren, A., et al. (2019). HyCREWW: A Hybrid Coral Reef Wave and Water level metamodel. *Computers & Geosciences*, *127*, 85–90. <https://doi.org/10.1016/j.cageo.2019.03.004>
- Rueda, A., Vitousek, S., Camus, P., Tomás, A., Espejo, A., Losada, I. J., et al. (2017). A global classification of coastal flood hazard climates associated with large-scale oceanographic forcing. *Scientific Reports*, *7*(1), 5038. <https://doi.org/10.1038/s41598-017-05090-w>
- Sallenger, A. H. J. (2000). Storm impact scale for barrier islands. *Journal of Coastal Research*, *16*(3), 890–895.
- Salmon, S. A., Bryan, K. R., & Coco, G. (2007). The use of video systems to measure run-up on beaches. *Journal of Coastal Research*, *50*, 211–215. Retrieved from <http://www.jstor.org/stable/26481585>
- SHOM. (2016). LITTO3D@ Guadeloupe.
- SHOM. (2020). Références Altimétriques Maritimes-édition 2020.
- Sous, D., Tissier, M., Rey, V., Touboul, J., Bouchette, F., Devenon, J. L., et al. (2019). Wave transformation over a barrier reef. *Continental Shelf Research*, *184*, 66–80. <https://doi.org/10.1016/j.csr.2019.07.010>
- Splinter, K. D., Carley, J. T., Golshani, A., & Tomlinson, R. (2014). A relationship to describe the cumulative impact of storm clusters on beach erosion. *Coastal Engineering*, *83*, 49–55. <https://doi.org/10.1016/j.coastaleng.2013.10.001>
- Stockdon, H. F., Holman, R. A., Howd, P. A., & Sallenger, A. H. (2006). Empirical parameterization of setup, swash, and runup. *Coastal Engineering*, *53*(7), 573–588. <https://doi.org/10.1016/j.coastaleng.2005.12.005>
- Symonds, G., Huntley, D. A., & Bowen, A. J. (1982). Two-dimensional surf beat: Long wave generation by a time-varying breakpoint. *Journal of Geophysical Research*, *87*(C1), 492–498. <https://doi.org/10.1029/JC087iC01p00492>
- Torres, R. R., & Tsimplis, M. N. (2012). Seasonal sea level cycle in the Caribbean Sea. *Journal of Geophysical Research*, *117*, C07011. <https://doi.org/10.1029/2012JC008159>
- Torres, R. R., & Tsimplis, M. N. (2014). Sea level extremes in the Caribbean Sea. *Journal of Geophysical Research: Oceans*, *119*, 4714–4731. <https://doi.org/10.1002/2014JC009929>
- Valentini, N., Balouin, Y., & Bouvier, C. (2020). Exploiting the capabilities of surfcam for coastal morphodynamic analysis. *Journal of Coastal Research*, *95*, 1333. <https://doi.org/10.2112/si95-256.1>
- Valentini, N., Saponieri, A., Danisi, A., Pratola, L., & Damiani, L. (2019). Exploiting remote imagery in an embayed sandy beach for the validation of a runup model framework. *Estuarine, Coastal and Shelf Science*, *225*, 106244. <https://doi.org/10.1016/j.ecss.2019.106244>
- Vetter, O., Becker, J. M., Merrifield, M. A., Pequignet, A. C., Aucan, J., Boc, S. J., & Pollock, C. E. (2010). Wave setup over a Pacific Island fringing reef. *Journal of Geophysical Research*, *115*, C12066. <https://doi.org/10.1029/2010JC006455>
- Vitousek, S., Barnard, P. L., & Limber, P. (2017). Can beaches survive climate change? *Journal of Geophysical Research: Earth Surface*, *122*, 1060–1067. <https://doi.org/10.1002/2017JF004308>
- Wandres, M., Aucan, J., Espejo, A., Jackson, N., De Ramon N'Yeurt, A., & Damlamian, H. (2020). Distant-source swells cause coastal inundation on Fiji's coral coast. *Frontiers in Marine Science*, *7*, 546. <https://doi.org/10.3389/fmars.2020.00546>
- Yao, Y., Huang, Z., Monismith, S., & Lo, E. (2012). Characteristics of monochromatic waves breaking over fringing reefs. *Journal of Coastal Research*, *29*(1), 94–104. <https://doi.org/10.2307/23353574>